NASA TECHNICAL MEMORANDUM

NASA TM X-62,297

WIND TUNNEL STUDIES OF MARTIAN AEOLIAN PROCESSES

Ronald Greeley, James D. Iversen, James B. Pollack, Nancy Udovich, and Bruce White

University of Santa Clara
Santa Clara, Calif. 95053

Iowa State University
Ames, Iowa 50010

and

Ames Research Center
Moffett Field, Calif. 94035

May 1973

WIND TUNNEL STUDIES OF MARTIAN AEOLIAN PROCESSES

Ronald Greeley[1]

James D. Iversen[2]

James B. Pollack[3]

Nancy Udovich[1]

Bruce White[2]

[1] Physics Department, University of Santa Clara, Calif. 95053
(Mail Address: Space Science Division, Ames Research Center,
National Aeronautics and Space Administration,
Moffett Field, Calif. 94035)

[2] Department of Aerospace Engineering, Iowa State University
Ames, Iowa 50010

[3] Space Sciences Division, Ames Research Center
National Aeronautics and Space Administration,
Moffett Field, Calif. 94035

WIND TUNNEL STUDIES OF MARTIAN AEOLIAN PROCESSES

ABSTRACT

In order to determine the nature of martian aeolian processes, an investigation is in progress which involves wind tunnel simulations, geologic field studies, theoretical model studies, and analyses of *Mariner 9* imagery; this report presents the preliminary results. Threshold speed experiments were conducted for particles ranging in specific gravity from 1.3 to 11.35 and diameter from 10.2 μ to 1290 μ to verify and better define Bagnold's (1941) expressions for grain movement, particularly for low particle Reynolds numbers and to study the effects of aerodynamic lift and surface roughness. Wind tunnel simulations were conducted to determine the flow field over raised rim craters and associated zones of deposition and erosion. A horseshoe vortex forms around the crater, resulting in two axial velocity maxima in the lee of the crater which cause a zone of preferential erosion in the wake of the crater. Reverse flow direction occurs on the floor of the crater. The result is a distinct pattern of erosion and deposition which is similar to some martian craters and which indicates that *some* dark zones around martian craters are erosional and some light zones are depositional. Analyses of the erosional and depositional zones associated with a 6 m raised rim crater on an open field and a 1.2 km natural impact crater tentatively confirm the wind tunnel results.

Application of the wind tunnel results to Mars indicates that for flat surfaces, free stream winds in excess of 400 km/hr are required for grain movement. However, lower velocities would be required in regions of high surface roughness, e.g., cratered terrain, and it is proposed that such

regions could be zones of origin for some martian dust storms. Analysis of the Coriolis effect on surface stress shows that surface streaks would be deflected about 15^{o} from the geostrophic wind direction at mid-latitudes.

INTRODUCTION

Dust storms and other aeolian activities have been suspected to occur on Mars on the basis of telescopic observations (deVaucoulers, 1954; Kuiper, 1957; Rea, 1964; and others) and theoretical considerations of the martian surface and atmosphere (Ryan, 1964; Sagan and Pollack, 1969). *Mariner 9* results confirm the existence of aeolian features on Mars and show that aeolian processes play a significant role in modifying the martian surface (Sagan et al., 1973). Many aeolian features were observed in various stages of formation as the martian dust storm of 1971-1972 slowly subsided (Sagan et al., 1972). Analyses of Mariner 9 imagery reveal many features that appear to have resulted from long-term aeolian processes (Masursky, 1973). Knowledge of martian aeolian activity as a geologic process is essential to the understanding of the complex surface characteristics and geologic history of the planet.

Martian aeolian features occur in a variety of forms, most of which are associated with craters or other topographic obstructions. The features are subdivided into two general types: dark streaks and light streaks (figures 1 and 2). During the Mariner 9 mission, several areas were imaged repetitively in order to observe possible surface changes. Figure 1 shows a crater 17 km in diameter that developed a dark fan-shaped streak within a 38 day period (Sagan et al., 1972); it is typical of many dark features. Figure 2 shows light streaks associated with craters. These and all light streaks imaged repetitively during the mission showed no observable changes. Sagan et al. (1972) concluded that the light streaks are comparatively stable and the dark streaks unstable. Both types of features apparently can be used as surface

wind direction indicators and some attempts have been made to derive global wind patterns from streak orientations (Sagan et al., 1973; Arvidson, in press).

Suspected aeolian features other than crater streaks include laminated terrain (Murray et al., 1972), erosional pedestal craters (McCauley, 1973), and irregular light and dark streaks withinin, on, and outside the rims of large craters. One irregular dark zone within a crater 150 km in diameter in Hellespontus was imaged by the Mariner 9 narrow angle (telescopic) camera and was revealed to be an intercrater dune field about 60 km x 30 km (Cutts and Smith, 1973). Thus, both erosional and depositional features of aeolian origin are observed on Mars.

Initial analyses of aeolian features on Mariner 9 images pose several basic questions regarding the martian aeolian regime:

1) What are the criteria that may be used to separate aeolian depositional from aeolian erosional features?

2) What is the aerodynamic flow field over craters and what are the geological implications of the flow field in terms of zones of erosion and deposition? Does the flow field change significantly with changes in crater geometry?

3) What are the important parameters governing the movement of particles by wind on Mars and how do these parameters differ from those on Earth? For example, what wind velocities on Mars are required for particle movement?

4) If the above three questions can be answered, is it possible to determine rates of erosion and deposition and particle size and/or composition of martian aeolian material from analyses of spacecraft data and theoretical considerations?

As a means of developing answers to these questions, an investigation is currently in progress that involves particle movement studies using an atmospheric wind tunnel, qualitative wind tunnel simulations of aeolian erosion and deposition associated with craters, theoretical model studies, and field

studies of possible terrestrial analogs. The investigation is a multi-disciplinary effort of a geologist, an aerodynamicist, and a planetary physicist. This report presents our preliminary results, which are presented in four sections. The first section involves wind tunnel studies of individual particle movement. The second section is an application of wind tunnel results to Mars in order to estimate wind velocities and to determine the effect of Coriolis forces on surface stress under martian conditions. Section three concerns qualitative wind tunnel simulations of wind patterns over craters and section four compares the wind tunnel results with full-scale features in the field.

Acknowledgments

This paper was orginally presented in part at the Royal Society of London discussion meeting (May, 1973) on the results of spacecraft missions to Mars. We wish to thank Sir Harrie Massey, Sec. R.S. and the staff of the Society for their efforts in preparing the meeting. Special thanks go to Dr. J.E. Guest, University of London Observatory, as the organizer of the meeting.

We wish to acknowledge Robert Haberle for his calculations of the geostrophic winds on Mars and David Wong for his assistance in some of the wind tunnel experiments.

This work was supported by the Office of Planetology Programs, National Aeronautics and Space Administration.

WIND TUNNEL STUDIES OF AEOLIAN PARTICLE MOVEMENT

Movement of particles by wind is a complex phenomenon. Bagnold's classic work (1941), based on wind tunnel studies and field observations, defines the basic parameters and relationships of sand movement by wind. Drawing on his results and employing conventional techniques of wind tunnel scaling, we have verified Bagnold's (1941) fluid threshold experiments and extended the data over a wider range of particle sizes and densities, especially as related to small grains for application to martian studies. We have not yet conducted *impact* threshold (saltating grains) and our results are restricted to discussion of fluid threshold experiments.

The important physical parameters describing aeolian processes are given in Table I. These parameters can be arranged in the form of dimensionless similitude parameters commonly used in wind tunnel simulations. A discussion of the similitude parameters as applied to aeolian processes is presented in Appendix I. Although it is not possible physically to satisfy all parameters simultaneously in the wind tunnel, each important parameter can be studied independently to determine its effect on the aeolian regime.

Because the surface pressure on Mars is significantly lower than on Earth, several facilities have been proposed in which martian dust storms could be simulated under reduced pressure (Bidwell, 1965; Chang et al., 1968). Using Bagnold's (1941) experimental data, Ryan (1964) and Arvidson (1972) made theoretical calculations of grain movement under martian conditions. Adlon et al. (1969) constructed a low-pressure wind tunnel and conducted grain movement studies at pressures corresponding to those of Mars. Although an exact experimental determination of certain parameters should be performed

TABLE I

GLOSSARY OF SYMBOLS FOR AEOLIAN PARAMETERS

A	Bagnold's coefficient, $V_{*_T}\sqrt{\frac{\rho_p\ g\ D_p}{\rho}}$
B	Particle friction Reynolds number at optimum diameter, $V_{*_T} D_p/\nu_{\rho T}$
C_L	Lift coefficient, $C_L = L / 1/2\rho v^2 S$
C_d	Drag coefficient, $C_d = D/1/2\rho V^2 S$
D	Drag force, (force)
D_c	Crater diameter (length)
D_p	Particle diameter (length)
e	Coefficient of restitution
g	Acceleration of gravity (length/time^2)
h	Ripple height or reference height (length)
ℓ	Length (length)
L	Reference length (length)
ℓ_t	Wake length (length)
L^*	Monin-Obhokhev Stability length, $L^* = V^3_* C_p \rho T/KgH$ (length) (where C_p is specific heat, T is temperature, H is heat flux at surface)
R	Reynolds number, VL/ν
S	Reference area (length^2)
t	Time (time)
T	Turbulence factor
V	Velocity (length/time)
V_*	Friction velocity, (=surface stress= $\sqrt{\tau / \rho}$ (length/time)
V_{*_t}	Threshold friction velocity (length/time)

V_F	Terminal velocity	(length/time)
V_∞	Free stream velocity	(length/time)
V_g	Geostrophic wind (above boundary layer)	
W	Weight	(force)
W_s	Sample width	(length)
x	Streamwise distance	(length)
y	Lateral distance	(length)
z	Vertical distance	(length)
z_o	Roughness length	(length)
z_o'	Roughness length in saltation	(length)
γ	Specific gravity	
δ	Boundary layer thickness	(length)
κ	von Kármán's constant (a so C_1)	
λ	Ripple wave length	(length)
μ	Absolute viscosity	(mass/length-time)
ν	Kinematic viscosity	(length^2/time)
ρ	Mass density of atmosphere	(mass/length^3)
ρ_p	Particle density	(mass/length^3)
τ	Shear stress	(force/length^2)

in a low-density wind tunnel, deposition and flow patterns over surface features (craters, etc.) can be modelled to some extent in a normal atmospheric boundary-layer wind tunnel (Bidwell, 1965), if close attention is paid to satisfying appropriate modelling parameters and to the wind tunnel boundary layer configuration. Examination of these parameters (Appendix I) shows that *most* of the important modelling parameters are more easily, and validly, satisfied in a normal atmospheric wind tunnel.

A series of wind tunnel experiments was designed to gain additional knowledge of particle movement by wind, especially as related to martian problems. Tests were conducted in an open-circuit environmental wind tunnel which has an adjustable ceiling in order to establish a zero pressure gradient. The test section is 6 m long with a 1.5 m^2 cross section; maximum speed is about 40 m/sec.

Threshold Friction Velocity Experiments

We will first discuss experiments conducted on a flat surface, which determines the minimum or threshold stress needed to set sand particles into motion. Rather than dealing explicitly with the threshold stress, τ_T , we will instead use the threshold friction velocity V_{*_T} , which by definition is related to τ_T by $\tau_T = \rho V_{*_T}^2$, where ρ is the fluid density. Operationally, V_{*_T} can be determined more directly through a measurement of the vertical velocity structure.

Bagnold has suggested that V_{*_T} can be expressed in terms of the other parameters of interest as:

$$V_{*_T} = A \sqrt{\frac{\rho_p - \rho}{\rho} g D_p} \qquad (1)$$

where ρ_p is particle density, g is acceleration due to gravity, D_p is the mean particle diameter, and A is a coefficient experimentally determined by Bagnold, who suggested that it was a function solely of the particle friction Reynolds number B. B is defined as

$$B = V_{*_T} d/\nu \qquad \text{(Bagnold, 1941)} \qquad (2)$$

where ν is the kinematic viscosity and d is the mean surface roughness which is on the order of the particle diameter, D_p. If this expression for V_{*_T} is correct, then in principle, all one needs to do to determine V_{*_T} for any environment is to measure A(B). Hence, one bar wind tunnels are just as valid as low pressure wind tunnels for applications to Mars with the appropriate correction for ν reflecting the lower martian atmospheric pressure.

Bagnold's coefficient A is constant for particles down to about 50 μ in diameter, then increases rapidly for smaller particles. This results, as Bagnold (1941) discovered, in an *optimum* particle size for which threshold speed is a minimum, corresponding to a certain value of particle friction Reynolds number. Bagnold's coefficient A for small particles was determined from limited experimental data, and only for quartz material.

Experiments to determine Bagnold's coefficient A for a wide range of particle diameters and densities were conducted and the results are shown in figures 3 and 4. That the data shown in figure 3 for a wide range of particle sizes all fall close to an unique line indicates the basic validity of Equation (1) for the threshold friction velocity and makes its application to Mars meaningful. According to Bagnold (1941), the value of the optimum diameter should scale as the density ratio, (ρ_p/ρ), to the (-1/3) power. The minimum threshold speed ratio should be directly proportional to the one-third power

of the density ratio. Limited data in figures 3 and 4 comparing copper particles and glass spheres corroborate these trends.

Making use of Equations (1) and (2), we obtain the following formulae relating the threshold friction velocity V_{*_T} and particle diameter D_p to A(B), B, ρ_p/ρ, g, and ν (assuming that $\rho_p >> \rho$ and $\frac{\rho_p - \rho}{\rho} \approx \frac{\rho_p}{\rho}$):

$$V_{*_T} = A^{2/3} (\rho_p \, g \, \nu \, B/p)^{1/3} \tag{3}$$

$$D_p = (B \, \nu/A)^{2/3} \, (\rho/\rho_p \, g)^{1/3} \tag{4}$$

Since A is simply a function of B, we can generate a curve of V_{*_T} as a function of D_p by picking a set of values of B and solving Equations (3) and (4). Thus, the desired curve can be generated without going through an iterative process, as would be required if Equations (1) and (2) were used. It should be noted that ν scales inversely as the fluid density ρ. The point on the curve in figure 3 where the relatively sharp break occurs (A = 0.146 and B = 0.38) corresponds to the minimum threshold friction speed. For values typical of an one-atmosphere wind tunnel, the values of minimum V_{*_T} and corresponding D_p were calculated for a range of values of particle density, using Equations (3) and (4) and the results are shown in figure 5. If a modelling material is chosen to correspond to minimum threshold speed, it is evident that if minimum diameter is desired, the material should be of high density. However, materials of lighter density will result in somewhat lower minimum threshold speeds.

Effect on Nonerodible Roughness and Lift on Threshold Speed

The *roughness height*, (z_o), or simply the roughness of a surface, is a

measure of the effective relief of a surface. This parameter plays a strong role in determining the vertical wind profile close to the surface, which in turn determines the value of the friction velocity for a given wind speed above the boundary layer. Above we have determined the threshold friction speeds for flat surfaces overlain solely with the sand particles being studied. Here we consider the effect of the presence of numerous, large, immovable objects on the surface. In this circumstance, the roughness height z_o is determined by the size of the large, nonerodible objects (to first approximation, z_o is 1/30 of the mean particle diameter, or the height above the surface at which the wind velocity is zero). Chepil and Woodruff (1963) observed that an increase in nonerodible roughness greatly increases the effective threshold speed. For a spherical particle resting on a bed of similar particles, a *lift force* acts through the center of the particle and a drag force (surface stress) acts at a distance $D_p/6$ above the sphere center (Chepil, 1958). Equating opposing moments of lift, drag, and weight,

$$V_{*_T} = 0.373 \sqrt{\frac{\rho_p \, g \, D_p}{\rho} \left[\frac{1}{1 + \frac{C_L}{9.6} \left(\frac{V}{V_*} \right)^2} \right]} \tag{5}$$

with a reference velocity for fully rough flow of $V = \frac{V_*}{0.4} \ln \left(1+\frac{D_p}{z_o}\right)$, the effective lift coefficient C_L is solved for by letting A = 0.117 (the asymptotic value in figure 3) and $D_p/z_o = 30$; thus for fully rough flow, A may be written as:

$$A = \frac{V_{*_T}}{\sqrt{\rho_p \, g \, D_p/\rho}} = \frac{0.373}{\sqrt{1 + 0.776 \left[\ln \left(1 + D_p/ z_o\right)\right]^2}} \tag{6}$$

It is assumed that the effective lift coefficient is unchanged for the other

values of D_p/z_o. If large nonerodible roughness elements are present (i.e., high relief), then the equivalent roughness height z_o becomes greater than $D_p/30$ and the coefficient A increases according to Equation (6).

To test the validity of Equation (6), values of threshold friction speed for several materials were determined for values of nonerodible equivalent roughness heights z_o of 0.0104 cm and 0.338 cm. The results of the experiments are shown in figure 6. Although there is quite a bit of data scatter, the results seem to substantiate the form of Equation (6). The letters NNR in figure 6 signify that no nonerodible roughness elements were present in those tests and that the ratio D_p/z_o is 30 (or slightly higher in the transition range). Figure 7 shows the threshold friction speed as a function of particle diameter for one of the test materials (heavy glass spheres). The bottom curve is derived from the curve of figure 3 and the other curves from Equation (6) and again the trend seems to be substantiated by the experimental results.

Although some investigators have ignored the effect of particle lift in attempting to predict threshold friction speed, the effect of lift is apparently important. Bagnold (1956, 1973) has stated that the initial upward acceleration of a particle (not struck by another particle) from the bed is due to a lift-force but that the lift force becomes very small shortly after the particle has lifted off the bed. The lift force is due to the very high mean velocity gradient very near the surface.

An effective lift coefficient at threshold was calculated from the data of figures 1 and 2. Although the results are rather tentative, initial calculations indicate the lift is an important parameter for particle threshold movement, particularly for low particle friction Reynolds numbers. However, additional work is required before a definitive statement can be made.

PREDICTED AEOLIAN CONDITIONS FOR MARS

Threshold Velocities

We now make use of our wind tunnel results to predict the threshold friction velocities for Mars. To do this, we make use of Equations (3) and (4) and the curves previously discussed that give the dependence of the Bagnold's coefficient A on the particle friction Reynolds number B. In addition we must specify the values of g, ρ_p, ρ, and ν appropriate for the conditions on Mars. The acceleration of gravity for Mars is approximately 375 cm/sec^2. We carry out our nominal calculations for a particle density of 2.7 gm/cc, a value typical of terrestrial sands. The value of ρ is obtained from the perfect gas equation for a specified value of surface pressure and an assumed air temperature of 240°K. Finally since the martian atmosphere is composed principally of carbon dioxide, we obtain the value of ν by dividing the dynamic viscosity of carbon dioxide, η, at 240°K (1.21 x 10^{-4} gm/cm/sec) by ρ. We note that for the conditions of interest η does not depend on ρ.

Figure 8 shows the dependence of threshold friction velocity upon particle diameter for a surface pressure of 5 mb, which is representative of the mean surface pressure for Mars. Also given is a similarly generated curve, which makes use of the values of A found by Bagnold (1941). We see that in a crude sense the two curves agree with one another. However, Bagnold's data imply friction velocities lower by about 20% than those implied by our wind tunnel data. In addition, the value of the particle diameter having the smallest threshold velocity is about twice as large for Bagnold's data as for ours. As discussed above, our data are much more complete near the

minimum in the threshold curve than were those of Bagnold. Our wind tunnel results show that the optimum (lowest wind velocity) diameter is about 300 microns at a surface pressure of 5 mb (compared with 200μ for 25 mb of Ryan, 1964).

Because substantial elevation differences are present on Mars, we have calculated the threshold friction velocity for several values of the surface pressure. Figure 9 shows the results of these calculations for values of the surface pressure of 2½, 5, and 10 mb. As can be seen, the threshold velocities are substantially lower for the high surface pressure case than for the low surface pressure case. In addition, the value of the particle diameter at the minimum in the threshold curve shifts to a somewhat smaller diameter as the pressure increases (in agreement with Ryan, 1964).

The above calculations were carried out for a particle specific gravity of 2.7, a value typical of terrestrial sands. However, it is conceivable that this value may vary somewhat, depending on the composition and prior history of the grains under study. For example, the specific gravity might be as high as 4 if the sand is particularly rich in iron, or it may be as low as 1 if the particles contain very fine pores, as might occur for volcanic ash. The latter seems somewhat unlikely based on terrestrial experiences, which indicate that porosity effects are important only for larger sized particles, because the pores generally are not as small as several microns. Figure 10 illustrates the dependence of particle size and threshold velocity on particle density for the minimum in the threshold curve. These results were obtained for our nominal case of 5 mb surface pressure. As the particle density increases, the threshold velocity increases and the particle size decreases. Thus, motion on Mars will occur most readily for sands having a

low density and will involve particles whose size is about 400 microns. For all the cases of surface pressure and particle density that seem likely for Mars, the particle size is on the order of several hundred microns at the minimum on the threshold curve. As we will see in the next sections, even for the minimum threshold friction velocity, the required wind speed to initiate motion is quite large. Thus, if particle motion is to occur with any sort of frequency on Mars, as seems to be the case, there should be a substantial population of grains whose size is several hundred microns. This inference about the size of the martian sand grains is in good agreement with values for most areas sampled by the Mariner 9 infrared radiometer (Kieffer, et al., 1973). This argument can be put in a somewhat different way. Sagan and Pollack (1969) have argued that those grains that are easily set in motion will eventually cover grains that are not unlike planet-wide conditions on Earth where oceans serve as settling traps for dust. As a result, there will be a substantial population of surface grains whose size is close to the size at the minimum in the threshold curve. This hypothesis seems to be valid for terrestrial sand deserts contained in closed basins. Sagan and Pollack have also pointed out that such sized particles will not go into suspension on Mars, and thus a second population of grains, of much smaller size, must be present on Mars to account for the particles put into suspension during the great dust storms. These particles are set into motion not directly by the winds, but indirectly by the impact of a saltating particles from the large size population.

Estimate of the Geostrophic Wind Velocity at Fluid Threshold and the Angle of Rotation Through the Boundary Layer

Csanady (1972) derived a set of expressions relating the wind V_g above the boundary layer to the friction velocity V_* and also derived an expression

for the rotation angle α between the wind above the boundary layer and the direction of the stress at the ground. The expressions are valid at mid-latitudes where the Coriolis force is important. Toward the Equator, α will tend toward zero, while the ratio of V_g/V_* may change somewhat. According to Csanady:

$$V_g / V_* = \frac{1}{\sqrt{C_d}} \tag{7}$$

$$\alpha = \sin^{-1} \left(11 \sqrt{C_d}\right) \tag{8}$$

where C_d is the drag coefficient. C_d in turn may be expressed as a function of two dimensionless parameters which take account of the roughness of the surface, the gravity, the Coriolis parameter, and the temperature difference between the ground and the air above it. In the case of Mars, there are large temperature differences between the ground and air above it near noon and at night. However, for the case of no nonerodible roughness elements, the roughness height is so small that the value of C_d is not greatly affected by the large variations from neutral stability. Using the graphs and equations of Csanady (1972), we estimate that $C_d \sim 5 \times 10^{-4}$ near the minimum in the threshold velocity curve at a pressure of 5 mb. Inserting this value in Equations (7) and (8), we find that at a surface pressure of 5 mb, the wind velocity must exceed approximately 110 m/sec (400 km/hr, or 0.4 times the speed of sound on Mars!) for grain motion to occur on a smooth, flat surface. Such a wind is comparable to the *highest* winds expected on Mars; thus, a general dust storm will not occur too frequently on Mars. Instead, more frequent grain motion events will occur near craters where the local friction velocity corresponding to a given calculated geostrophic wind can be as much

as 2 or 3 times as large as that for a flat terrain.

The angle α found from the above calculation is 15^{o}. At midlatitudes, above the boundary layer the Coriolis force is balanced by the pressure gradient force, while within the boundary layer, both the Coriolis force and frictional forces balanced the pressure gradient force. Thus, above the boundary layer, the wind is approximately parallel to isobars, while within the boundary layer, the wind direction gradually changes direction so it has a component directed towards lower pressure. As a result there will be a slight angle α between the direction of surface stress and geostrophic wind (see Halton, 1972). The geostrophic wind is to the right of the surface streak in the northern hemisphere and to the left in the southern hemisphere. This factor needs to be taken into account in analyzing streak directions. Angle α decreases in latitudes toward the Equator. The above estimate of α should at present be considered only as an approximate value since it is very difficult to model all the factors that influence α in the boundary layer. The above estimate of V_g is better established.

MODELLING OF AEOLIAN PROCESSES ASSOCIATED WITH CRATERS

A series of experiments is in progress in order to simulate aeolian processes associated with craters. In contrast to the experiments described in the first section, these experiments are qualitative and were made without regard to problems of scaling to full-size structures under martian conditions. The experiments are progressing along three lines: 1) aeolian deformation of craters modelled in loose sand, 2) loose sand blown over solid crater (non-deformable) models, and 3) studies to determine the influence of crater geometry on the size, shape, and position of zones of erosion and deposition associated with craters.

Each experiment is described as a *run*. Sequential still photographs and time-lapse motion pictures were made during each run. All still photographs are oriented with the illumination from the upper left-hand corner and the wind direction from the left toward the right. Unless otherwise indicated, wind velocities were obtained with a hot-wire anemometer in the free stream above the model. Quartz sand, 120μ in diameter was used in most of the experiments.

Craters Subject to Aeolian Deformation

This series of experiments involves craters of two geometries, raised-rim craters and nonraised-rim craters, molded in loose 120μ sand and subjected to steady winds. The objective was to determine the zones of preferential erosion and deposition around the crater and to determine the progressive geometric distortion of the crater. For some of the runs in this series, longitudinal (parallel to wind direction) and transverse profiles were obtained to determine the changes in surface relief.

Run 21. Figure 11 shows sequential photographs for Run 21 in which a non-raised-rim crater (bowl-shaped depression in the sand) was subjected to wind of 307 cm/sec velocity. The crater outline in plan view became progressively ovoid, with the axis parallel to the wind direction. Sand ripples were only slightly deflected as they passed the lateral edges of the crater. There is a zone in the lee of the crater in which no ripples formed and the surface remained undisturbed. This area is probably analogous to the "shadow zone" of full-scale sand dunes, in which relatively little erosion occurs.

Run 12. Figure 12 shows sequential photographs for Run 12 in which a raised-rim crater (in contrast to Run 21) was subjected to relatively low velocity (250 cm/sec) wind. In a manner similar to Run 21, sand ripples passed around the crater rim and merged at a point about 3/4 of the crater diameter in the lee of the crater, forming a triangular-shaped shadow zone. In plan view, the crater assumes an ovoid outline pointing upwind. Figure 13 shows sequential longitudinal profiles in which the windward and leeward crater rims became asymmetric during the run, as would be expected. Although the entire crater migrated downwind, the upwind rim moved more rapidly (causing the ovoid outline to progressively flatten, figure 12), while the deepest part of the crater (the original crater center) remained fixed in place. From this and subsequent runs, it was concluded initially (Greeley, 1972) that a raised-rim crater formed entirely in loose sand could be treated as a combination parabolic dune (windward rim) and barchan dune (leeward rim) in regard to erosional and depositional patterns This conclusion, however, was an oversimplification that does not account for other, more complex aeolian patterns that develop in association with craters.

Run 8. Figure 14 shows the sequential development of Run 8 in which all conditions were identical to Run 12 except the wind velocity which was nearly

double (approximately 450 cm/sec). The last picture in the sequence represents nearly stable conditions, i.e., no significant changes occurred after this time-frame. As in Run 12, the crater became ovoid and developed a leeward shadow zone. At this higher velocity, however, depressions developed in the lee of the lateral crater rims. The depressions are erosional and evidently represent zones of relatively high wind velocity. They apparently result from vorticies shed from the crater rim, as will be discussed below.

Figure 15 is a comparison of Run 8 results to a small crater imaged by Mariner 9 in Mare Tyrrhenum. The surface wind direction arrow shown for the Mars picture was derived from crater tail streaks over a wide geographic range in this area. The dark zones correspond to the erosional depressions of Run 8, both in their position and relative size as compared to the crater diameter. By analogy, we infer that the lateral dark zones on the martian crater are the result of aeolian erosion. Similar dark zones occur on small craters in other regions of Mars.

Figure 15 also shows a similarity in crater outline of Run 8 and the martian crater. Both features are ovoid, pointing directly upwind and it is tempting to infer that the martian crater deformation resulted from aeolian processes.

Data from additional runs involving raised-rim craters molded in loose sand showed that, as the velocity is increased, the lateral erosional depressions lengthen. At highest velocities (700-800 cm/sec) it was not possible to determine definitive patterns because sand ripples formed very quickly and overrode the crater and lateral erosional depressions. For higher velocities, solid crater models and loose sands were used.

Solid-Model Crater Experiments

This series of runs involves craters modelled as solid forms that were not subject to deformation, in contrast to the series described in the previous section. Three general types of experiments were conducted with solid models: 1) loose sand introduced into the free stream upwind of the model and allowed to saltate across the model and collect in zones of deposition, 2) models in which the crater was filled to the rim with loose sand (other areas free of sand) and subjected to wind erosion, 3) crater and surrounding floor covered by loose sand and subjected to wind. In all three cases craters with raised-rim geometries were used.

Run 29. Figure 16 shows the sequential filling of a solid-model raised-rim crater with sand which was introduced into the free stream upwind of the model. Sand initially collected in the down-wind part of the crater floor (figure 16, "A"), then migrated (arrow) across the floor toward the left (in the opposite direction from the free stream flow direction) and collected in the lee of the windward crater rim (figure 18, "B"). This *reverse flow* on the crater floor was observed in all experiments of this configuration. Simultaneously with the sand deposition within the crater, sand collected on the upwind side of the windward crater rim (figure 16, "C"). Eventually, sand was eroded from the zone of deposition at "B" and was carried over both lateral rims (figure 16, "D"); other sand grains were carried over the leeward rim and deposited in the immediate lee of the crater rim (figure 16, "E"). Free stream velocity for Run 29 was 435 cm/sec. The run was terminated after relatively stable conditions ensued.

Similar runs at higher free stream velocities produced essentially the same patterns of deposition, except that the amount of sand collected in each zone was less than that at the lower speed.

Run 32. Figure 17 shows the sequential development of a solid-model crater (same model as used in Run 29, figure 18) in which the crater was filled to the rim with 120 μ sand (other surfaces free of sand). As the run progressed, sand was initially eroded from the downwind part of the crater interior and redeposited in essentially that same pattern that developed for Run 29. The run continued until stable conditions ensued; free stream velocity was 285 cm/sec. At higher speeds, the same pattern developed except that less material remained in the crater.

Run I-F-14. Figure 18 shows the sequential erosion of a solid-model crater and surrounding surface that were buried to a depth of 1 cm with 200μ glass particles. The bilobate pattern of erosional depressions is similar to the pattern of Run 8 (figure 14). Subsequent experiments under a variety of conditions confirmed the common development of bilobate erosional depressions off the lateral rims of raised-rim craters. We believe that the wind pattern over the is similar to wind patterns observed over small protuberances (with small height-to-diameter ratios) in boundary layers, as described by Gregory and Walker (1951) and Sedney (1972) for laboratory scale tests. If so, there would be a *horseshoe vortex* wrapped around the leading edge of the crater rim with the trailing vortices emanating downstream from the crater sides. The axes of the vortices are parallel to the wind direction. The bilobate erosional depressions can be accounted for by the scouring action of the vortices. The tangential component of velocity in each trailing vortex is outward away from the crater wake centerline near the surface, and inward above the vortex cores. The axial velocity components near the surface just downstream from the crater rim would be minimum on the wake centerline with maximum velocities on either side of the wake of greater magnitude than outside the wake zone.

Preliminary results indicate that as the velocity increases, the size, shape, and position of the bilobate erosional zones change. Generally, higher free-stream velocities cause the erosional zones to lengthen, widen, and shift their position toward the crater wake centerline until they eventually merge and form one large erosional zone in the lee of the crater (figure 19). This may be accounted for by the fact that, far downstream, the two axial velocity maxima merge, thus developing a *maximum* wind speed on the crater wake centerline. A triangular-shaped deposition zone remains in the immediate lee of the crater. It must be emphasized, however, that parameters other than wind velocity can change the shape and position of the trailing vortices. These parameters include time, crater height-diameter ratio, and others; their effects are currently being studied.

Runs 217, 218, and 219. Figure 20 shows the sequential erosion for Run 217 of a raised-rim solid model (crater and base) that was covered with a thin layer of 120 μ sand *glued* to its surface (in order to provide a roughness equivalent to the diameter of the loose sand); the entire model was then covered with *loose* sand and subjected to wind. Free stream velocity was 572 cm/sec. Bilobate erosional zones developed in a pattern similar to Run 8 and I-F-14 (figures 14 and 18). The run was continued until stable conditions were obtained, at which point nearly the entire model floor was swept free of loose sand by wind. Sand remained in the floor zone of the crater and in a pike-shaped zone in the lee of the crater.

Figure 21 shows the sequential photographs for Run 218, which was identical to Run 217, except that the free stream velocity was initially 330 cm/sec and gradually increased (only after stable conditions ensued for each incremental increase) to a final velocity of 695 cm/sec. Again, the bilobate erosional zones developed. At the higher velocity (695 cm/sec) the

pike-shaped sand zone in the lee of the crater was reduced in size and the bilobate erocional zones became more pronounced. Run 219 was a continuation of Run 218 except that the free stream velocity was increased to 838 cm/sec. Under the higher velocity the sand zone in the lee of the crater formed a distinctive trilobate pattern. Sand also remained on the upwind side of the windward crater rim and in the crater floor zone. Erosion occurred in the downwind part of the crater floor as noted in previous runs.

Figure 22 compares the results of Run 219 with a small (about 2 km in diameter) martian raised-rim crater in the region northwest of Memnonia. The surface wind arrow was derived from crater streaks in the region. The trilobate light-colored pattern of the martian crater bears a striking resemblance in regard to its shape and relation to the crater and wind direction to the sand deposits of Run 219, suggesting that the light material in the wake of the martian crater is the result of deposition, rather than erosion. The suggestion is further enhanced by the presence of a white zone on the upwind side of the windward rim of the martian crater, and the dark zone in the wake of the crater beyond the trilobate light pattern. The dark zone would correspond to the zone of erosion resulting from the merging of the axial velocity maxima along the wake centerline, as described above. While the interpretation that the white zones of the martian crater are depositional, we do not imply that all white streaks associated with martian craters are depositional. The pattern illustrated in figure 22 is rare in the Mariner 9 images (it is on a "B" frame, and, hence, represents a very small sample surface).

Crater Erosion-Deposition Zone Studies

A series of wind tunnel experiments (Runs 37-169) was conducted to determine the effect that craters have on threshold free stream velocities compared to flat surfaces free of topographic obstructions. This series permitted the definition of zones of relative erosion and deposition as related to the crater. Using the solid model raised rim crater described for Runs 217-219, small patches of 120 μ sand were placed individually (one patch for each run) on a systematic grid (figure 23) over the model. For each run, the wind speed was slowly increased in graduated steps until the first sand grains began to move consistently (threshold), as observed through a telescope. The wind speed at this point is the threshold free stream velocity for the sand as related to a particular location in, on, or near the crater. Low threshold free stream velocities represent relative erosion (grains easily moved); high threshold free stream velocities represent relative deposition. In addition, observations were made for specific grain movement directions in order to determine surface stress direction over the model. The results of this series are discussed by zones identified on figures 23 and 24.

Zone 1. Points on the grid (figure 23) close to the crater had higher threshold free stream velocities than those farther upwind. The crater rim is a bluff body (a broad surface facing the wind) which resists the passage of air. Upwind of the crater the external airstream begins to "feel" the obstruction and a positive pressure gradient forms in front of the crater. Some of the fluid particles (air) will be slowed down, some will be stopped, and others will be reversed. Reverse flow by sand grains was observed at the front rim of the crater. A point of attachment was close to the bottom of the windward crater rim (figure 24). Above the point grains were carried up and

over the rim; at the level of the point, the grains moved sideward; and below the point grains were moved downward in reverse flow. The sideward motion resulted from the horseshoe vortex around the crater rim.

Zone 2. Regions on the flanks of the crater had relatively lower threshold free stream velocities, evidently due to vortices. A horseshoe wortex wraps around the side of the crater, similar to that described by Gregory and Walker (1951) for pill box structures.

Zone 3. The downwind side of the leeward rim is a zone of relative deposition. Sand was carried over the leeward crater rim from regions of lower threshold free stream velocity. Particles deposited here were subsequently eroded more slowly (after the sand source was diminished).

Zone 4. Downwind from the crater the threshold free stream velocity is low and relatively constant, signifying a region of vortex action. The air stream which flows over the leeward rim and curls down meets the horseshoe vortex, resulting in a region of high erosion. The air on either side of this region is apparently unaffected by the crater and free stream velocities required to move particles were on the order of 20-25% greater than those inside the wake zone.

Zone 5. Air flow within the crater appears to be very complex. Loose sand on the upwind part of the leeward rim was carried by reverse flow across the crater floor, opposite to the main wind flow and deposited in the lee of the windward rim. Within the crater, the leeward rim is a region of erosion while the windward rim is a region of deposition.

TERRESTRIAL FIELD STUDIES OF AEOLIAN ACTIVITY ASSOCIATED WITH CIRCULAR BASINS

As a means of validating the preliminary laboratory determinations of the flow field over craters, aeolian processes associated with larger circular basins on Earth are currently being studied. These include: 1) raised-rim crater 6 m in diameter dug in a plowed field, 2) review of Wolf Creek Crater, Australia, a meteorite impact crater 1.2 km in diameter, and 3) Eagle Cove, Idaho, a semicircular basin 5.6 km in diameter which contains an extensive sand dune field. In each case, the primary interest is in determining the aerodynamic flow field over the structure and in determining zones of aeolian erosion and deposition.

Artificial Raised-Rim Crater

A raised-rim crater 6 m in diameter was dug in loose soil on a flat field of the Iowa State University campus prior to the Winter, 1972. The objective was to determine relative zones of erosion and deposition shown by drifted snow patterns following major snow storms of known wind velocity and direction. Triangular-shaped deposits of snow accumulated in the immediate wake of the crater and bilobate patterns of erosional zones formed in the same configuration observed in the wind tunnel simulations. The modelling parameters in this particular field test were estimated to be $V(h)^2 g D_c = 0.4$ (based on same relative h/L as the wind tunnel, $V_F/V_{*_T} = 5.0 \pm 3$, and $V(h)/V_F = 4.0 \pm 1$, $V(h) = 450$ cm/sec. Similar results were observed after several other snow storms.

Wolf Creek Meteorite Crater, Australia

Wolf Creek Crater is an impact structure about 1.2 km in diameter, formed in bedded quartzite (McCall, 1965). It has a distinct raised rim (figure 25)

and is surrounded by relatively flat sand plains. Its geometry, the existence of aeolian materials, and wind from a prevailing direction make it an ideal structure for determining flow fields over large-scale craters. Figure 26, adapted from McCall (1965, figure 3a,b), shows the approximate ovoid crater outline oriented to the prevailing wind direction and the zones of erosion and deposition. Sand deposits are on the upwind side of the windward rim, on the floor of the crater, in a horseshoe pattern wrapped around the crater rim and trailing downwind, and in a zone in the immediate lee of the crater rim. Zones of erosion are indicated by McCall (1965, figure 3a,b) as areas in which the aeolian material has been swept free, exposing the underlying bedded quartzite. These areas form a bilobate pattern between the zones of sand accumulation. The overall resulting pattern is essentially the same as derived in wind tunnel simulations.

Eagle Cove, Idaho

Eagle Cove, Idaho, is an old meander loop of the Snake River (figure 27) above 5.6 km in diameter, previously described (Greeley et al., 1971, Murphy and Greeley, 1972). The subcircular basin contains a large central sand dune and several small, complex dune fields. Eagle Cove is a settling basin for wind-borne particles carried by the prevailing northwest winds. A secondary wind direction is 180° to the prevailing wind and is evidently responsible for maintaining the large dune in the center of the basin, rather than against one wall of the crater as might be expected if only one dominant wind direction were involved (Murphy and Greeley, 1972).

The size and distribution of aeolian deposits in relation to Eagle Cove and the prevailing wind directions have implications for the interpretation of martian aeolian features associated with craters and eroded circular

basins. The central sand dune is nearly the same height as the basin rim and contains a small crater-like blowout; as such, it could be identified on low-resolution spacecraft imagery as the central peak of an impact crater, or a constructional feature of a volcanic crater. Thus Eagle Cove offers an alternative explanation for positive features in craters subjected to aeolian processes and bimodal wind directions.

In addition to the large central dune and inter-basin dune fields, Eagle Cove has a large sand dune field draped over the windward rim onto the basin floor. Many of the martian craters have similar distributions of dark zones on the crater rims and it has been demonstrated (Cutts and Smith, 1973) that some of the crater-associated dark zones are dune fields. In the case of Eagle Cove, the dune field is on the *upwind* side of the crater.

SUMMARY AND CONCLUSIONS

Studies of aeolian processes are currently in progress along three general lines: parametric wind tunnel studies of grain movement, wind tunnel simulations of the aeolian modification of craters, and field studies of possible terrestrial analogs. From these studies we are attempting to determine the general flow field over craters in order to define aeolian deposition and erosion patterns and to derive the influencing parameters for the application of the results to the martian aeolian regime. Initial results from these studies are applied tentatively to the interpretation of selected martian surface features.

Threshold speed (restricted to *fluid* threshold) experiments have been conducted in an atmospheric wind tunnel in order to:

1) Verify Bagnold's (1941) expressions for the aeolian movement of particles by extending the empirically derived data over a wider range of particle specific gravities (1.3 to 11.35) and particle diameters (8μ to 1290μ).

2) Better define particle movement by wind in the range of particles with low particle friction Reynolds numbers, important for martian applications.

3) Study the effects of nonerodible roughness and lift on particle motion.

Using the results from these experiments in combination with the appropriate parameters for Mars, predictions are made for martian aeolian conditions. Threshold velocities as a function of particle size were calculated for three atmospheric surface pressures on Mars, 2.5 mb, 5.0 mb and 10.0 mb. As the pressure decreases (corresponding to higher topographic elevations), the optimum particle size (corresponding to minimum wind velocity) increases. For a nominal pressure of 5 mb, optimum particle size is about 300μ; the

corresponding geostrophic wind to set the grains in motion of flat surfaces without topographic obstructions is extremely high, on the order of 400 km/hr. However, near craters the local friction velocity can be increased 2 or 3 times over that of a flat terrain. It is interesting to note that the proposed Viking '75 landing sites are on smooth, flat plains where the friction velocity will be lower and hence subject to less aeolian activity.

Coriolis effect on streak orientations must be taken into account in attempting to determine global wind patterns from surface features. In mid-latitudes on Mars, the deflection of the wind is about 15^{o} to the right of streak orientations in the northern hemisphere and 15^{o} to the left in the southern hemisphere.

Several qualitative wind tunnel simulations have been conducted over crater models. A general flow field has been derived tentatively for one raised-rim crater geometry and the associated zones of relative aeolian erosion and deposition determined. As the turbulent boundary layer approaches the crater rim, it begins to "feel" the obstruction and a pressure gradient develops which causes reverse flow of wind-transported material in front of the crater. In addition, a horseshoe vortex wraps around the crater rim, forming two trailing vortices off the lateral flanks of the crater with the vortex cores parallel to the surface. Two axial velocity maxima occur to the lee of the crater on either side of the wake centerline. Under certain conditions (e.g., high wind velocities), the two velocity maxima merge on the crater wake center line to form a zone of high surface stress. Flow *over* the crater is extremely complex and is only partly defined at this time; however, reverse flow occurs across the crater floor.

The flow field described above results in a pattern of aeolian erosion and deposition which appears to be characteristic for raised-rim craters. Deposition zones are as follows: 1) upwind side of the windward crater rim, 2) in the lee of the windward crater rim, resulting from material carried over the rim directly, and from material deposited by the reverse flow across the crater floor, and 3) in a trilobate pattern in the lee of the crater. Erosion zones include the upper areas of all windward-facing parts of the crater rim, the downwind part of the crater floor, a zone off both lateral flanks of the crater rim (corresponding to the position of the horseshoe vortex), and, in some cases, a zone along the centerline of the wake downwind from the crater.

Although we have not as yet determined all the important scaling parameters for simulating aeolian processes on Mars, it would appear that the problem of scaling from wind tunnel models to full size craters on Earth may not be so great, as evidenced by the existence of essentially the same patterns of relative erosion and deposition in wind tunnel simulations as was observed for the 6 m, artificially constructed crater and the 1.2 km impact crater (both raised-rim structures).

The shape and position of the defined zones and their relation to the crater geometry and prevailing wind direction have been applied to the interpretation of suspected aeolian features associated with martian craters. In some cases, dark zones appear to be the result of erosion and light zones the result of deposition. In other cases (e.g., the intercrater dune field of Cutts and Smith, 1973) dark areas result from deposition. In addition, although the examples are not discussed here, some of our wind tunnel simulations would indicate that some light zones could result from erosion. Thus,

both light and dark zones can result from either relative erosion or relative deposition. While it may be possible to identify the process on the basis of morphology in some cases (e.g., figure 22), other parameteas should also be considered. The *relative luminance,* or the degree of lightness or darkness of a surface, depends upon several factors that are influenced by aeolian activity. These include grain size, grain composition, and ripple wave length. Zones of high wind speed, or relative erosion, could result in large grains, long ripples, or concentrations of high-density material. Although some work has been done to study the effect of grain size on relative luminance, the three main velocity-dependent parameters (grain size, ripple length, composition) have not been taken into account in combination. It is apparent that until the relative effects of grain size, ripple length, and mineral composition *taken in combination* are determined, it will not be possible to fully understand aeolian processes on Mars.

Although not all modelling parameters can be satisfied in the wind tunnel, a great deal of information can be gained about the nature of the flow field and the resulting depositional and erosional features. A systematic series of experiments is currently underway, in which each of the major modelling parameters is varied independently, to determine its effect upon eolian features. This is being done by varying crater diameter, tunnel speed, and modelling material. The results will not only enable us to determine effects of each similitude parameter, but will also assist greatly in later numerical experiments in which all modelling parameters can be satisfied.

APPENDIX I

MODELLING AEOLIAN PHENOMENA

Several wind tunnel installations have been constructed to investigate the effects of wind on sand and soil movement. The primary facility for studying the transport of sand by wind was that of Bagnold (1941). Experiments conducted in his wind tunnel resulted in curves and equations for threshold friction speed and mass transport of sand due to wind. Another facility used mostly for studying wind erosion of soil is described by Chepil and Woodruff (1963). Other wind tunnels for the study of soil and sand transport by wind have been built (Ford, 1957; Malina, 1941).

The structure of the turbulent planetary boundary layer on Earth has been studied extensively (e.g., Lumley and Panofsky, 1964; Plate, 1971). Jensen (1958) and others have observed that the lower portion of the planetary boundary layer (in a neutrally stratified atmosphere) follows the logarithmic law

$$\frac{V(z)}{V_*} = \frac{1}{K} \ln \frac{z}{z_o} \tag{1}$$

where V_* is the friction velocity and k is von Kármán's constant ($K \cong 0.4$). Jensen showed that for simulation of the atmospheric boundary layer, the roughness parameter for the wind tunnel floor must scale with the roughness parameter in nature, i.e.,

$$\frac{z_{o_M}}{z_o} = \frac{L_m}{L} \tag{2}$$

Most investigators have relied on the long test section to simulate the turbulent boundary layer profile so the model is immersed in the boundary

layer (Davenport and Syumov, 1968; Cermak, 1971). However, it is possible, although perhaps not as desirable, to produce thick boundary layers with the proper scaled velocity profiles in shorter test sections (Owen and Zienkiewics, 1957, Counihan, 1969, Sundaram, et al., 1972). Effects due to a nonneutral atmosphere (stable or unstable) can be simulated to some extent by cooling or heating the tunnel floor (Cermak, 1971).

In order to overcome some of the problems in scaling from wind tunnel models to full-scale features, important parameters describing aeolian processes can be arranged in the form of dimensionless similitude parameters.

1.	$\frac{D_p}{L}$	length
2.	$V(h)/V_F$	reference to particle terminal speed ratio
3.	$[V(h)]^2/gL$	Froude number
4.	e	coefficient of restitution
5.	ℓ/L	topographic geometric similarity
6.	z_o/L	roughness similitude
7.	z_o'/L	roughness similitude in saltation
8.	h/L	reference height similitude
9.	z_o/L^*	stability parameter
10.	λ/L	ripple length similitude
11.	V_F/V_{*_T}	particle property similitude
12.	$V_{*_T} D_p/\nu$	particle friction Reynolds number
13.	V_*/V_{*_T}	friction speed ratio
14.	ρ/ρ_p	density ratio
15.	$V(h)t/L$	time scale

The first four of these parameters have been suggested by Strom and Gerdel (1961) as the scaling parameters of primary importance in the modelling of accumulation of wind-driven snow and could thus also be important in modelling accumulation of dust particles from a dust storm. Some of the parameters are interrelated. The roughness height in saltation, z_o', for example, has been assumed by different investigators to be proportional to particle diameter (Zingg, 1953), to ripple wavelength (Bagnold, 1941), or to the square of particle terminal speed ($z_o' \sim V_F^2/g$, Owen, 1964). Thus parameter 7 $\left(z_o' /L \right)$ would be proportional to parameter 1 $\left(D_p/L \right)$, parameter 10 $\left(\lambda/L \right)$, or to the ratio of parameter 3 to the square of parameter 2 $\left(V_F^2/gL \right)$. In the latter case since (Bagnold, 1941)

$$V_{*_T} = A \sqrt{\frac{\rho_p g D_p}{\rho}} \tag{3}$$

the parameter z_o' /L would be related to parameters 1, 11, and 14

$$\frac{z_o'}{L} \sim \frac{V_F^2}{gL} = A^2 \frac{\rho_p}{\rho} \left(\frac{D_p}{L} \right) \left(\frac{V_F}{V_{*_T}} \right)^2 \tag{4}$$

Some of the listed modelling parameters may be combined by using the equation of motion for the particle. Since the flow pattern near a crater and in the crater wake is related to the crater diameter, the vertical equation of motion, for example, is made dimensionless by using the dimensionless variables $\bar{Z} = Z/D_c$ (where Z is the vertical displacement) and $\bar{t} = V(h)t/D_c$. The equation becomes

$$d^2 \bar{Z}/dt^{-2} = -3/4 \, C_D \left(\frac{\rho D_c}{\rho_p D_p} \right) \bar{V} \left(\bar{W} - d\bar{Z}/d\bar{t} \right) - gD_c/V(h)^2 \tag{5}$$

where $\bar{V}$ is the dimensionless relative speed and $\bar{W}$ the dimensionless vertical

air speed. Thus the dimensionless motion is a function of the three parameters $\rho D_c / \rho_p D_p$, $V(h)^2/gD_c$, and the particle Reynolds number.

Consider the modelling parameters:

1. $\rho D_c / \rho_p D_p$. By varying particle density and diameter and the crater diameter, this parameter can be varied from about 0.8 to 3. On Mars, this parameter would vary in value from about 1 for a 100 meter diameter crater to 100 for a 10 kilometer crater.
2. $V(h)/V_F$. Since the threshold friction speed V_* is proportional to the reference velocity V(h), providing geometry (including roughness) is exactly modelled, the ratio of reference velocity V(h) to terminal speed V_F will be modelled exactly if the ratio V_*/V_F is satisfied and if h/L is satisfied.
3. $[V(h)]^2/gL$. The Froude number cannot always be satisfied in the wind tunnel without having a tunnel speed far below threshold speed. It is desirable to make it as small as possible. Again since V_* is proportional to V(h), this is equivalent to requiring a modelling material with as small a threshold speed as possible. The value of this parameter varies from 10 to 150 in the wind tunnel, and from approximately 20 for a 100 meter diameter crater to 0.2 for a 10 kilometer crater.
4. e. The coefficient of restitution is satisfied if model and atmospheric materials have equivalent elastic properties.
5. ℓ/L. Topographic features should be scaled exactly to satisfy this criterion. At large distances upstream from the region of interest, it is probably only necessary to have equivalent scaled aerodynamic roughness.

6. z_o/L. The aerodynamic roughness should, in general, be to scale (Jensen, 1958). Except for those craters surrounded by large-scale ejecta or other rough surface features, this is probably small on Mars. If the corresponding model surface in the wind tunnel is too smooth, it may be necessary to distort this parameter in order to obtain a turbulent boundary layer. It is important at the same time, to insure that the ratio h/L be satisfied.

7. Z_o'/D_c. If the equivalent roughness height in saltation Z_o' is proportional to particle diameter, this parameter obviously cannot be satisfied on the laboratory scale model, since such fine particles would have a very high threshold speed. Also, if introduced into the air stream, the particles would go into suspension and the saltation process would not occur. Calculations of saltation trajectory, however, show that the maximum height during saltation would be several times larger on Mars than on Earth, just as the saltation height on Earth is several times as large in air as it is in water. If the equivalent roughness Z_o' is proportional to V_F^2/g, then z_o'/D_c is proportional to $\rho_p D_p/\rho D_c$, the inverse of the first parameter.

8. h/L. The reference height h at which the reference speed is measured should be located within the logarithmic portions of the wind tunnel and atmospheric boundary layers.

9. z_o/L^*. With a 'naturally' developed boundary layer in the wind tunnel, a boundary layer velocity profile is achieved which corresponds to a neutrally stratified atmosphere, for which the Monin-Obhukov length L^* is infinite and the ratio z_o/L^* is zero. A finite

value of L^* is achieved in the wind tunnel by heating or cooling the floor to obtain unstable or stable stratification. Another way of obtaining a nonneutral velocity profile in the wind tunnel (but perhaps not correct modelling of turbulence characteristics) would be by means of shear fences, graded grids, or the like (Counihan, 1969).

10. λ/L. The relative ripple length may be related to z_o'/L and the same comments apply.

11. V_F/V_{*_T} and 12. $V_{*_T} D_p/\nu$. As will be shown above, for a given condition such as for a modelling particle of diameter corresponding to minimum threshold speed, these two parameters would have the same values as for minimum threshold speed material on Mars.

13. V_*/V_{*_T}. The manner in which particles are transported and, in particular, the amount of material which is moved is a function of this ratio. Thus, in order to keep V_* as small as possible because of the Froude number, the threshold friction speed of the particle should be small.

14. $V(h)t/L$. The time scale in the wind tunnel is much shorter than the time necessary for pattern development on Mars since the characteristic time is the ratio of characteristic length L to reference velocity V(h). The time necessary for pattern development on Mars can thus be predicted from wind tunnel tests.

15. A Reynolds number $V(h)L/\nu$ may or may not be an important modelling parameter. For turbulent flows over sharp-edged features, the flow is relatively independent of Reynolds number. The critical model Reynolds number (above which effects are independent of

Reynolds number) depends upon model shape. If the model is too streamlined so that the test Reynolds number is below the critical, the model may have to be distorted by roughening the surface, creating sharper edges, etc. in order to lower the critical Reynolds number. Snyder (1972) quotes critical Reynolds number for sharp-edged cubes of 11,000 and 79,000 for a hemisphere-cylinder. In the current tests, Reynolds numbers based on crater diameter were generally above these values for sharp-rimmed model craters.

The listed parameters are easier to satisfy or will come closer to satisfaction in the one atmosphere wind tunnel than in the low density tunnel. Thus, for modelling aeolian features on martian topography, the low density wind tunnel should not be used.

REFERENCES CITED

Adlon, G. L., Weinberger, R. K. and McClure, D. R. 1969. Martian sand and dust storm simulation and evaluation. National Aeronautics and Space Administration CR 66882.

Arvidson, R. E. 1972. Aeolian processes on Mars: Erosive velocities, settling velocities, and yellow clouds. Geol. Soc. Amer. Bull., v. 83, p. 1503-1508.

Arvidson, R. E. In press. Wind-blown streaks, splotches, and associated craters on Mars: Statistical analysis of Mariner 9 photographs. Icarus.

Bagnold, R. A. 1941. The Physics of Blown Sand and Desert Dunes. Methuen and Co., Ltd., London, 265 p.

Bagnold, R. A. 1956. The flow of cohesionless grains in fluids. Phil. Trans. Royal Society, A, v. 249, p. 239-297.

Bagnold, R. A. 1973. The nature of saltation and of 'bed-load' transport in water, Proc. Royal Soc. London, A, v. 332, p. 473-504.

Bidwell, J. M. 1965. Notes on Martian sandstorms. Martin Marietta Corp. Report 1610-68-34.

Cermak, J. E. 1971. Laboratory simulation of the atmospheric boundary layer. Amer. Inst. Aeronautics Astronautics Jour., v. 9, p. 1746.

Chang, T. S., Lucas, W. C. and Youngblood, W. W. 1968. Laboratory simulation of the Mars atmosphere, a feasibility study. National Aeronautics and Space Administration, CR-61168.

Chepil, W. S. 1958. The use of evenly spaced hemispheres to evaluate aerodynamic forces on a soil surface. Trans. Amer. Geophysical Union, v. 39, p. 397.

Chepil, W. S. and Woodruff, N. P. 1963. The physics of wind erosion and its control. Advances in Agronomy, v. 15, p. 211-302.

Counihan, C. 1969. An improved method of simulating an atmospheric boundary layer in a wind tunnel. Atmospheric Environment, v. 3, p. 197-214.

Csanady, G. T. 1972. Geostrophic drag, heat and mass transfer coefficients for the diabatic Ekman layer. J. Atmospheric Sciences, v. 29, p. 488-496.

Cutts, J. A. and Smith, R. S. U. 1973. Eolian deposits and dunes on Mars. J. Geophysical Res., v. 78, p. 4139-4154.

Davenport, A. G. and Syumov, N. I. 1968. The application of the boundary layer wind tunnel to the prediction of wind loading, in Wind Effects on Buildings and Structures, v. 1, Univ. Toronto Press.

deVaucoulers, G. 1954. Physics of the Planet Mars. Faber and Faber Ltd., London.

Ford, E. F. 1957. The transport of sand by wind. Trans. Amer. Geophysical Union, v. 38, p. 171-175.

Greeley, R. 1972. Laboratory simulation of eolian-modified craters - preliminary report. Trans. Amer. Geophysical Union, v. 53, p. 427.

Greeley, R., Koscielniak, D. E. and Hodge, D. S. 1971. Bruneau sand dune field, Idaho, and its possible implications in martian geology. Trans. Amer. Geophysical Union, v. 52, p. 860.

Gregory, N. and Walker, W. 1951. The effect on transition of isolated surface excrescences in the boundary layer. Great Britain, Aeronautical Research Council, Reports and Memoranda No. 2779, p. 1-23.

Halton, J. 1972. An Introduction to Dynamical Meteorology. Academic Press, p. 87.

Jensen, M. 1958. The model-law for phenomena in natural wind. Ingeniøren, v. 2, p. 121.

Kuiper, G. P. 1957. Visual observations of Mars, 1956. Astrophys. Jour., v. 125, p. 307-317.

Lumley, J. L. and Panofsky, H. A. 1964. The Structure of Atmospheric Turbulence. Wiley, New York, 239 p.

McCall, G. J. H. 1965. Possible meteorite craters - Wolf Creek, Australia and analogs. Annals, New York Acad. of Sciences, v. 123, Art. 2, p. 970-998.

McCauley, J. F. 1973. Mariner 9 evidence for wind erosion in the equatorial and mid-latitude regions of Mars. J. Geophysical Res., v. 78, p. 4123-4137.

Malina, F. J. 1941. Recent developments in the dynamics of wind erosion. Trans. Amer. Geophysical Union, Pt. II, p. 262.

Murphy, J. D. and Greeley, R. 1972. Sand dunes at Eagle Cove (Bruneau), Idaho: Possible analogs to martian eolian features. Trans. Amer. Geophysical Union, v. 53, p. 1035.

Murray, B. C., Soderblom, L. A., Cutts, J. A., Sharp, R. P., Milton, D. J., and Leighton, R. B. 1972. Geological framework of the south polar region of Mars. Icarus, v. 17, p. 328-345.

Owen, P. R. and Zienkiewics, H. K. 1957. The production of uniform shear flow in a wind tunnel. J. Fluid Mechanics, v. 2, p. 521-531.

Plate, E. J. 1971. Aerodynamic characteristics of atmospheric boundary layers. Atomic Energy Commission Critical Review Series.

Rea, D. G. 1964. The darkening wave on Mars. Nature, v. 201, p. 1014-1015.

Ryan, J. A. 1964. Notes on the Martian yellow clouds. J. Geophysical Research, v. 69, p. 3759-3770.

Sagan, C. and Pollack, J. B. 1969. Windblown dust on Mars. Nature, v. 223, p. 791-794.

Sagan, C., Veverka, J., Fox, P., Dubisch, R., Lederberg, J., Levinthal, E., Quam, L., Tucker, R., Pollack, J. B., and Smith, B. A. 1972. Variable features on Mars: Preliminary Mariner 9 television results. Icarus, v. 17, p. 346-372.

Sagan, C., Veverka, J., Fox, P., Dubisch, R., French, R., Gierasch, P., Quam, L., Lederberg, J., Leventhal, R., Tucker, R., Eross, B., and Pollack, J. B. 1973. Variable features on Mars II: Mariner 9 Global Results. J. Geophysical Res., v. 78, p. 4163-4196.

Sedney, R. 1973. A survey of the effects of small protuberances on boundary-layer flows. Ames. Inst. Aeronautics Astronautics Jour., v. 11, p. 782-792.

Snyder, W. 1972. Similarity criteria for the application of fluid models to the study of air pollution meteorology. Boundary Layer Meteorology, v. 3, p. 113-134.

Strom, G. H. and Gerdel, R. W. 1961. Scale simulations of a blowing snow storm. Proc., Inst. Environmental Science, v. 53, p. 53-63.

Sundaram, T. R., Ludwig, G. R., and Skinner, G. T. 1972. Modelling of the turbulence structure of the atmospheric surface layer. Amer. Inst. Aeronautics and Astronautics Journal, v. 10, p. 743-750.

Zingg, A. W. 1953. Wind tunnel studies of the movement of sedimentary material. Proc. Fifth Hydraulic Conference, Bull. 34, Univ. Iowa Studies in Engineering, p. 111-135.

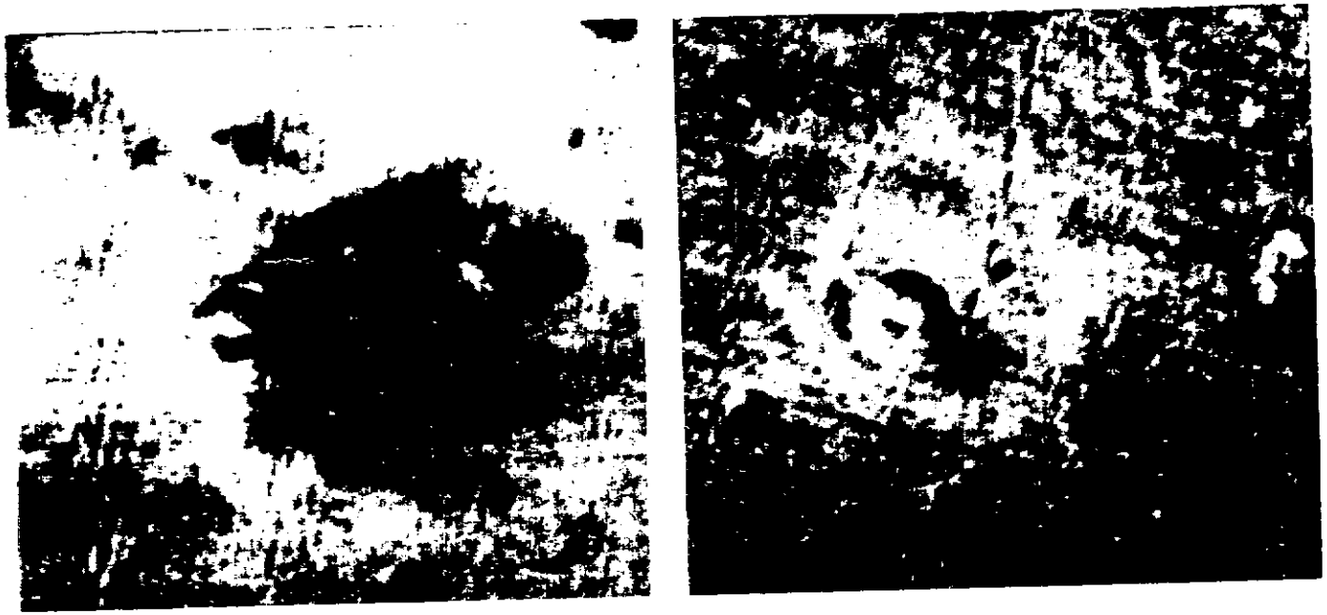

Figure 1. Crater 17 km in diameter in the Daedalia region near Solis Lacus, photographed on two revolutions (Rev. 115 on left, Rev. 195 on right). The dark fan-shaped feature developed in a period of 38 days (from Sagan et al., 1972).

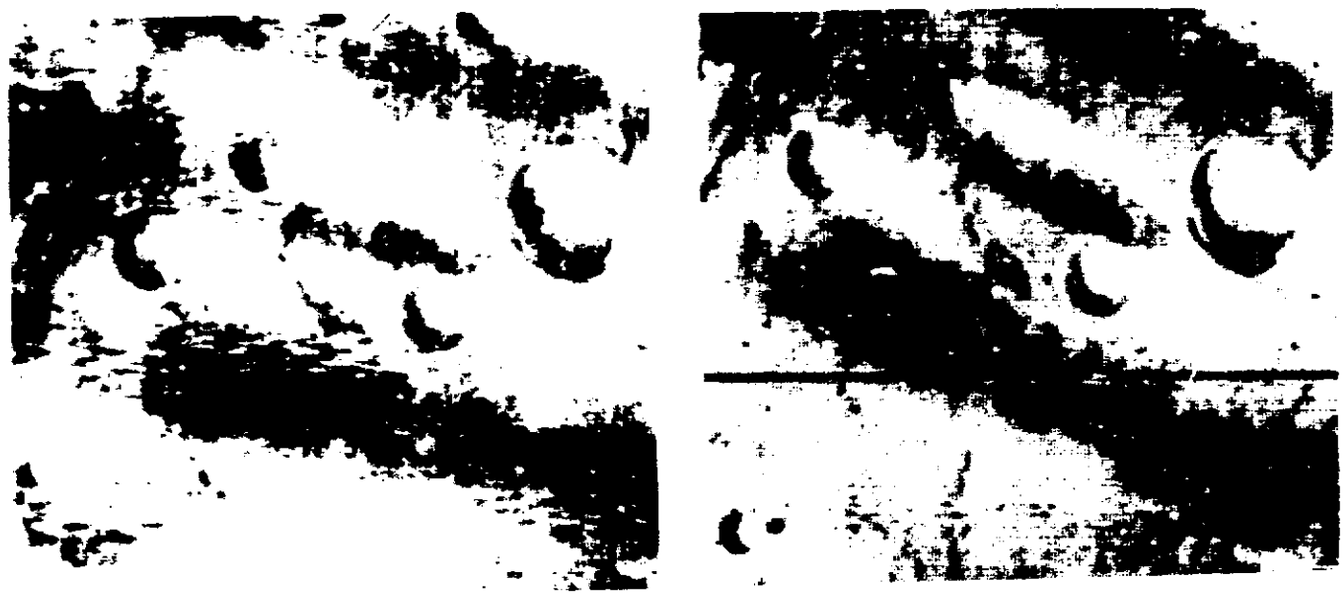

Figure 2. Cratered terrain in Hesperia, photographed on two revolutions (Rev. 128 on left, Rev. 167 on right), showing typical light streaks associated with craters and their apparent stability, compared to dark streaks (figure 1). Difference in contrast is the result of image processing (from Sagan et al., 1972).

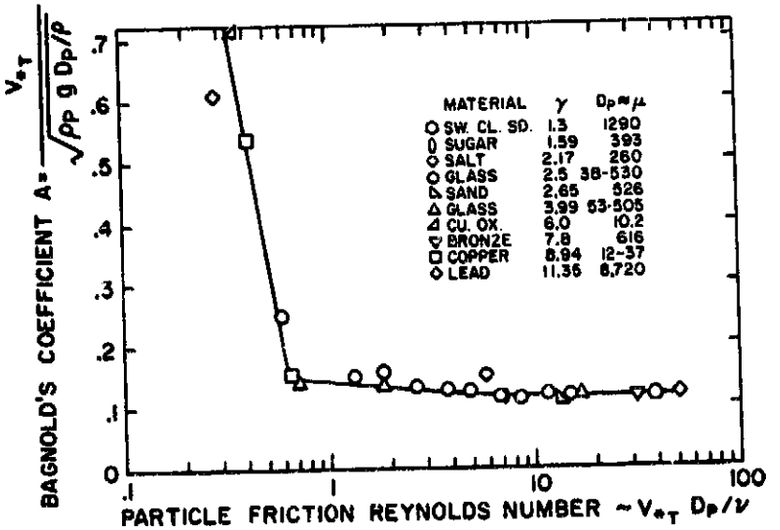

Figure 3. Threshold speed parameter ratio vs particle friction Reynolds number. SW.CL.SD. = sweet clover seed; CU.OX. = copper oxide particles.

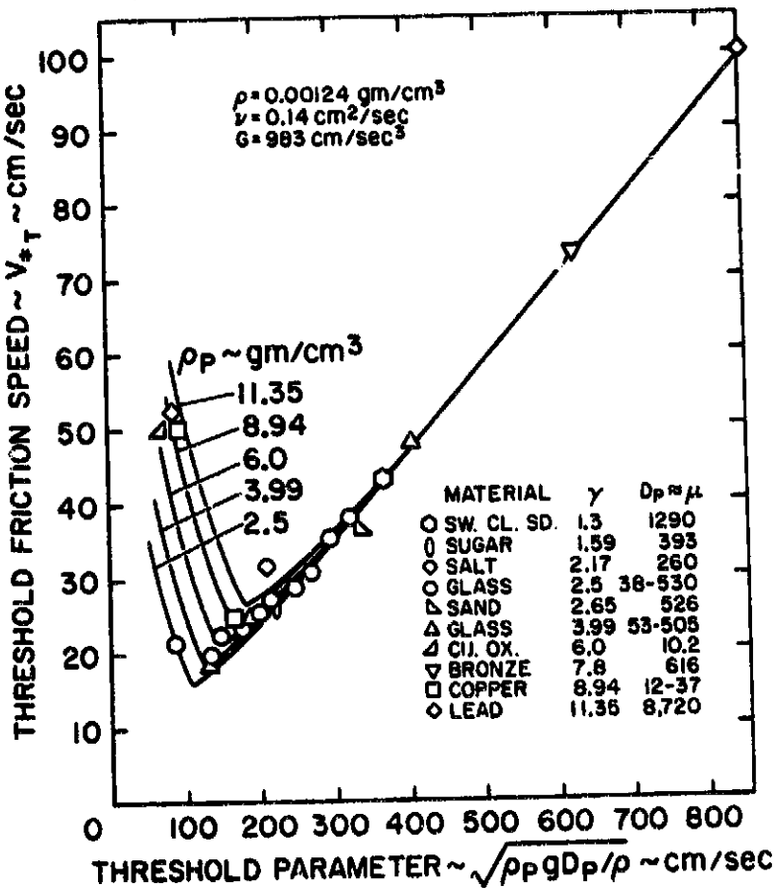

Figure 4. Threshold friction speed vs threshold parameter. SW.CL.SD. = sweet clover seed; CU.OX. = copper oxide particles.

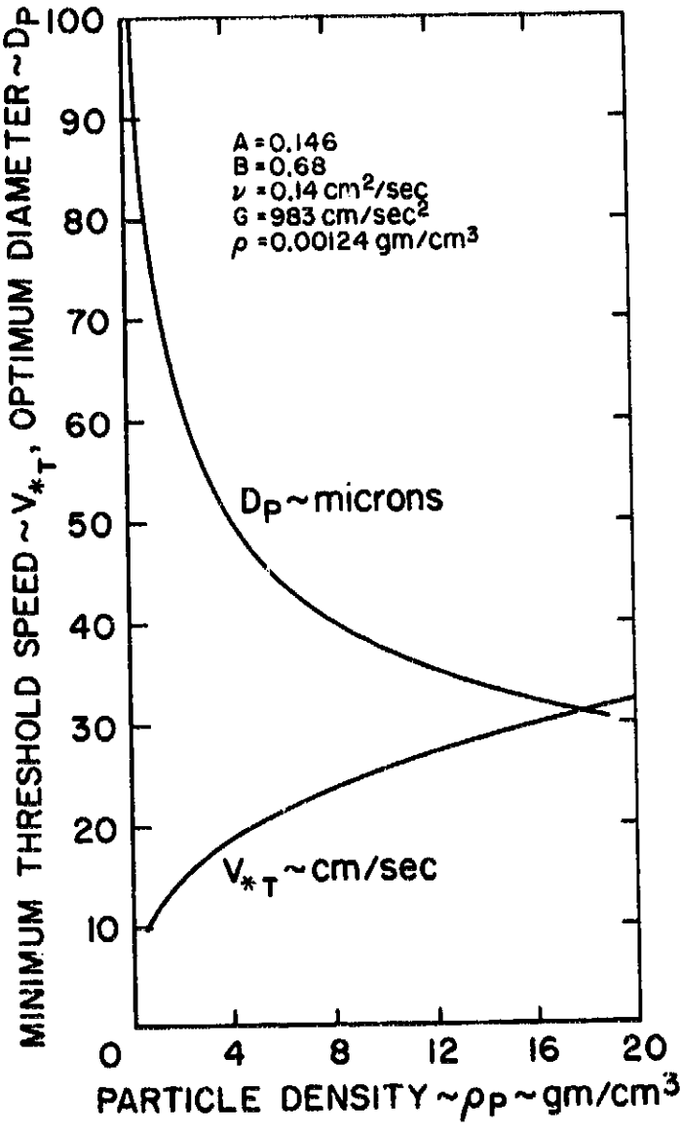

Figure 5. Variation with density of particle diameter and threshold friction speed for minimum threshold speed.

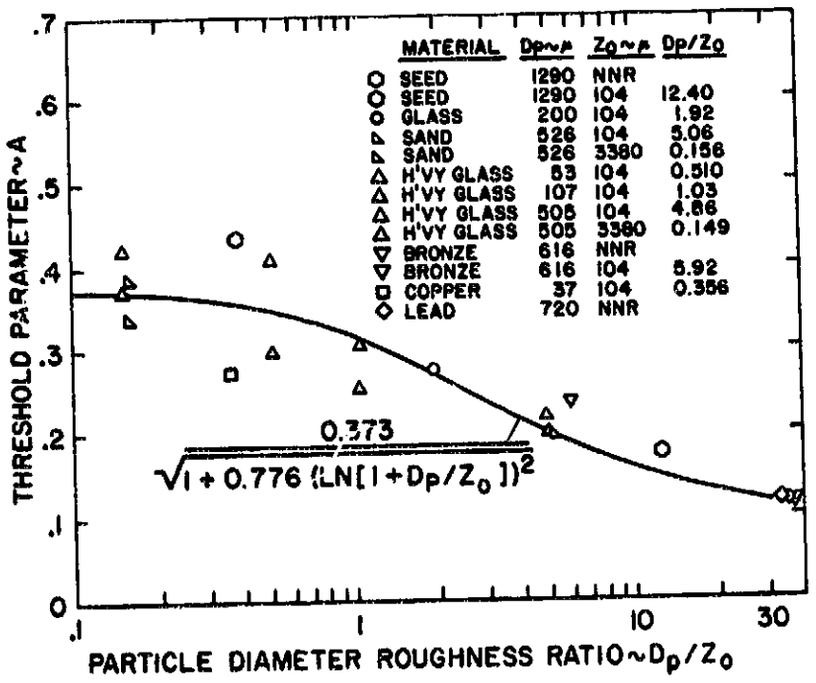

Figure 6. Threshold speed parameter ratio vs ratio of particle diameter to nonerodible roughness height. NNR = no nonerodible roughness.

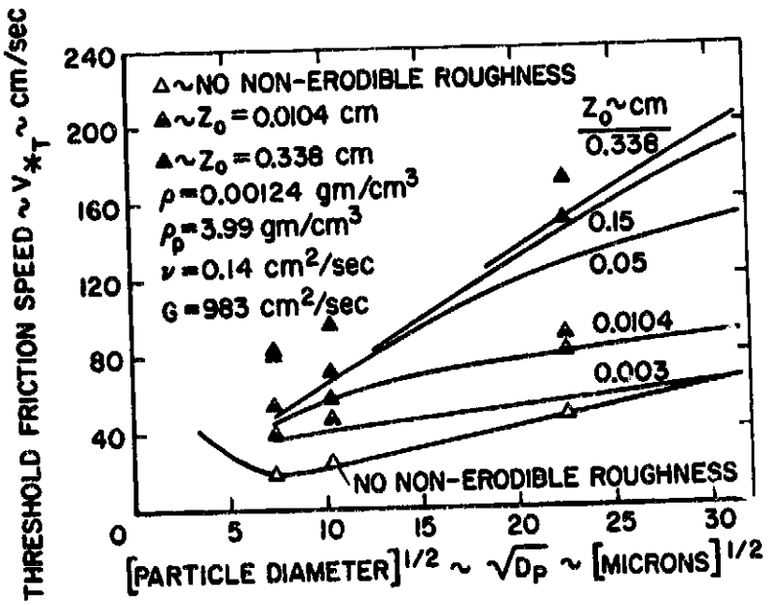

Figure 7. Threshold friction speed as a function of particle diameter including effect of nonerodible roughness.

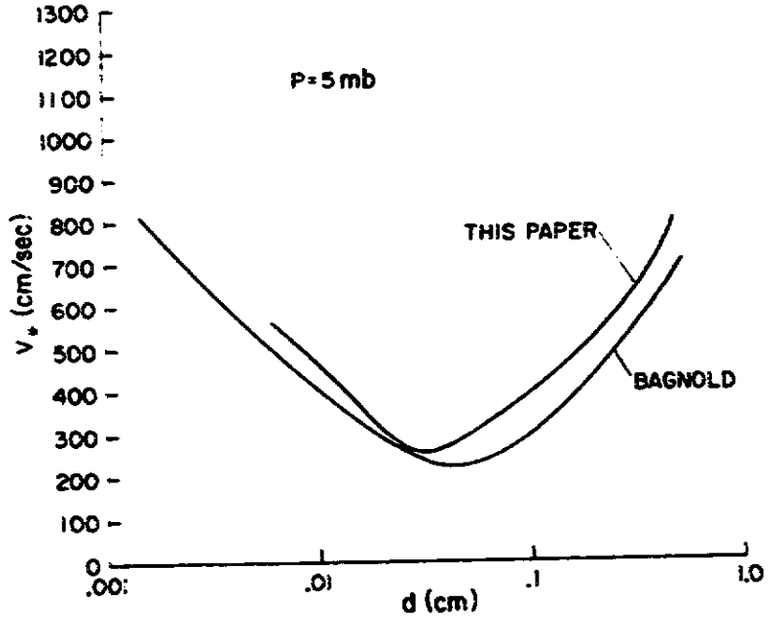

Figure 8. Threshold friction velocity as a function of particle size for a martian surface pressure of 5 mb. The two curves represent calculations made with the data reported in this paper and that given by Bagnold.

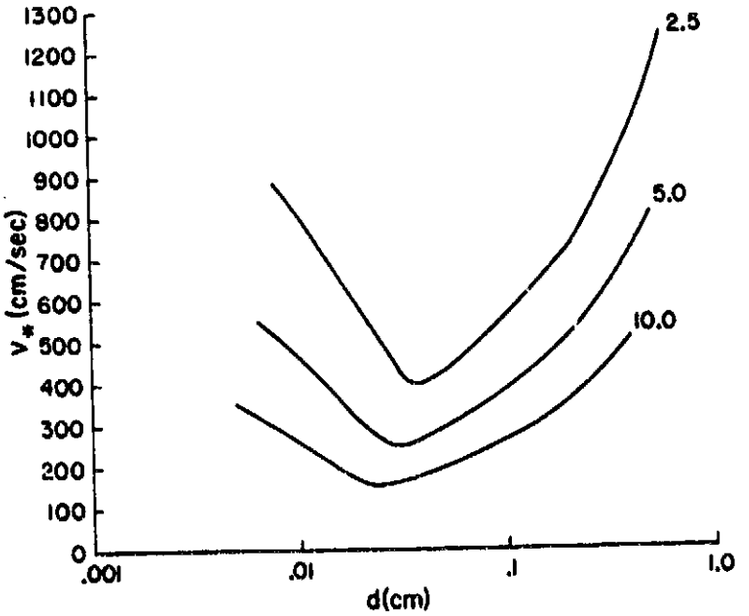

Figure 9. Threshold friction velocity as a function of particle size for martian surface pressures of 2-1/2, 5, and 10 mb.

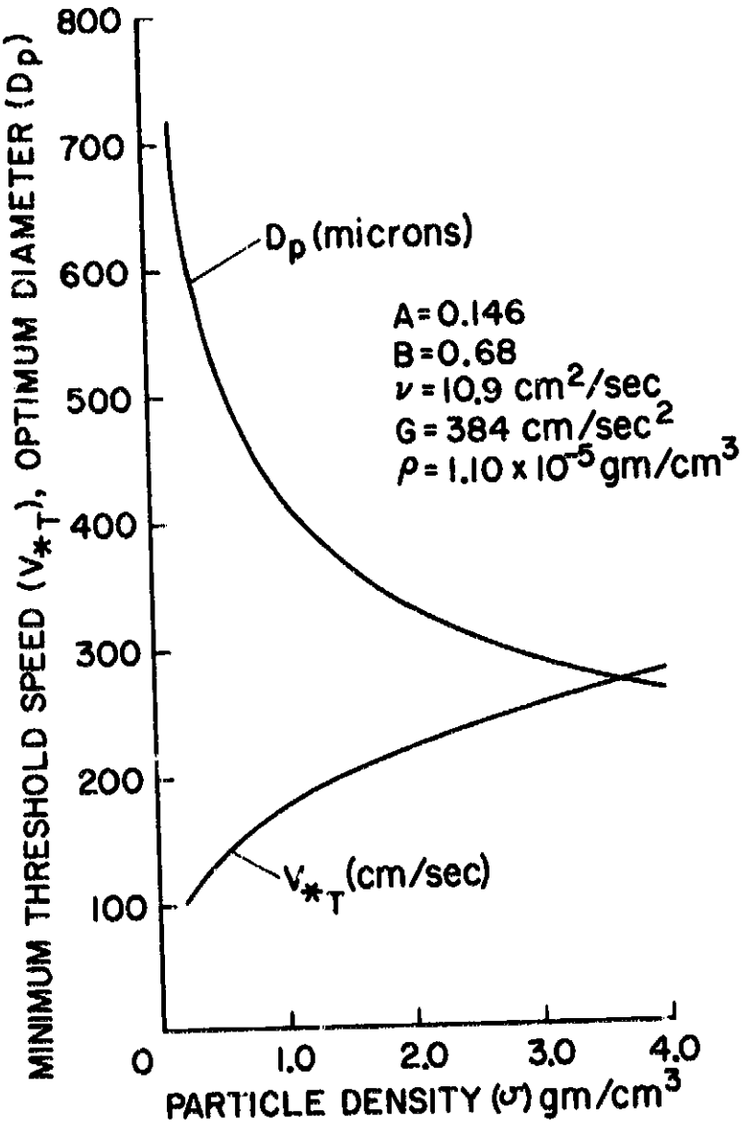

Figure 10. Particle diameter and threshold friction velocity (~cm/sec) as a function of particle density as the location of the minimum in the threshold curves. The calculations were carried out for a martian surface pressure of 5 mb.

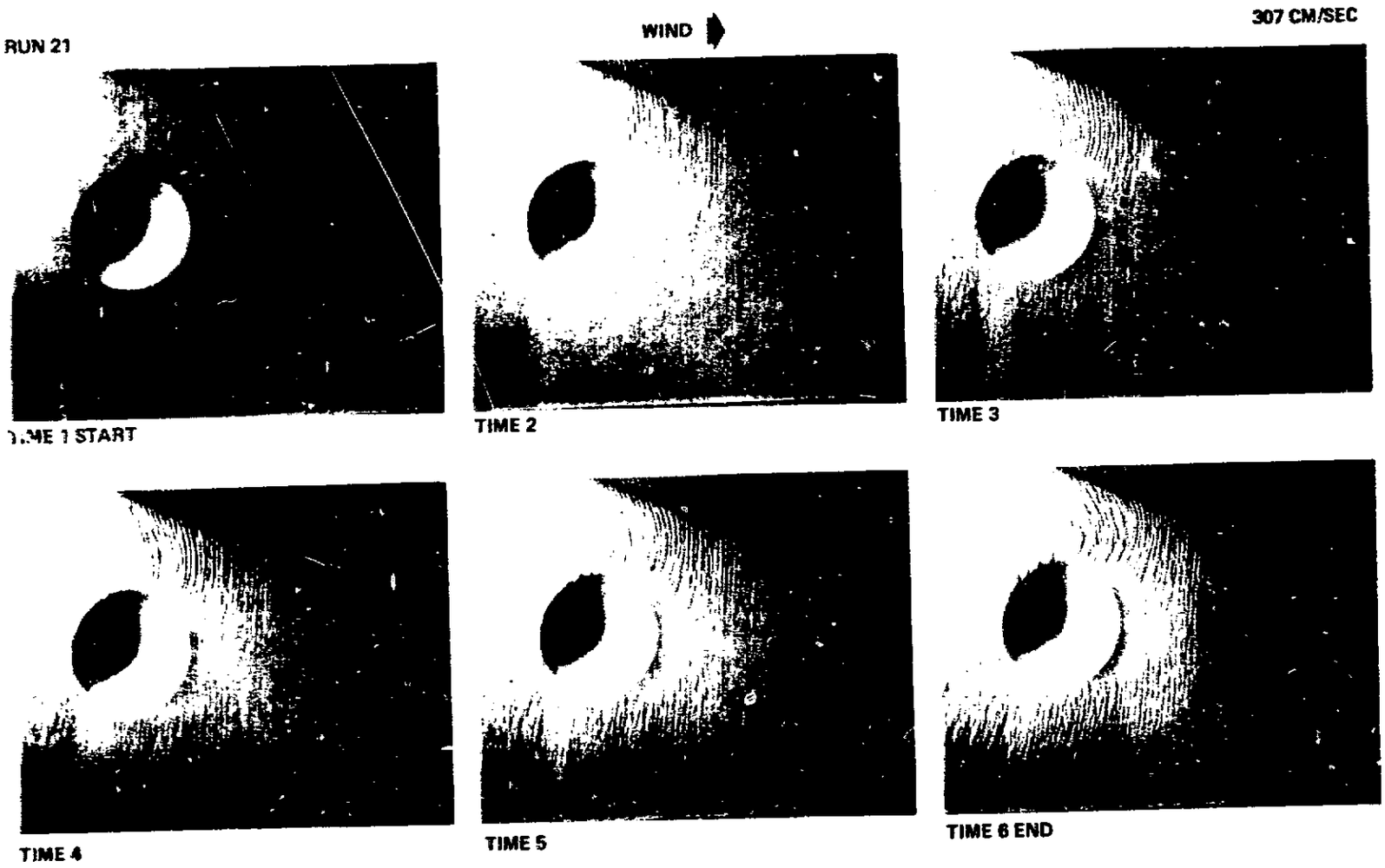

Figure 11. Run 21 wind tunnel simulation of aeolian deformation of a bowlshaped crater (nonraised-rim) molded in loose 120μ sand. Diagonal dark streak is a lighting artifact.

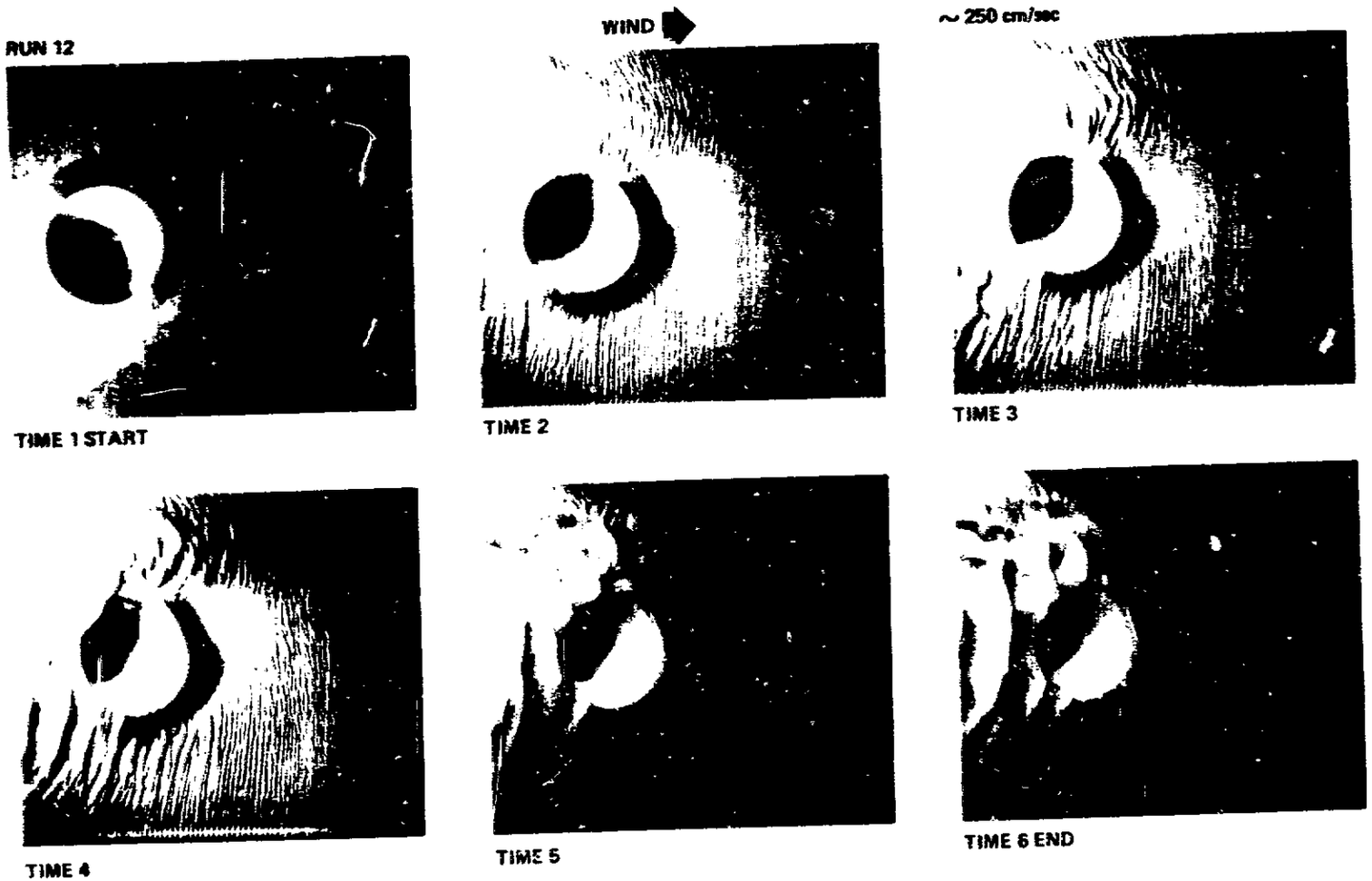

Figure 12. Run 12 wind tunnel simulation of aeolian deformation of a raised-rim crater molded in loose 120u sand. Diagonal dark streak is a lighting artifact.

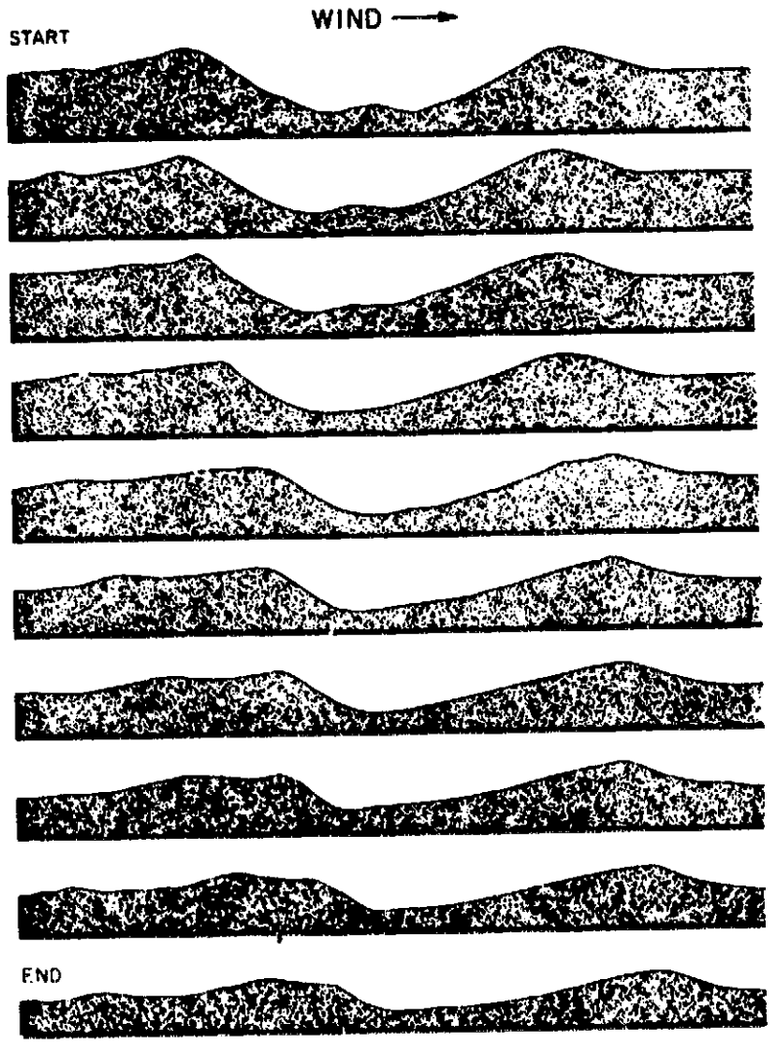

Figure 13. Sequential profiles of Run 12 (figure 12), taken parallel to the wind direction, showing downwind migration of crater rims and relative stability of deepest part of crater floor.

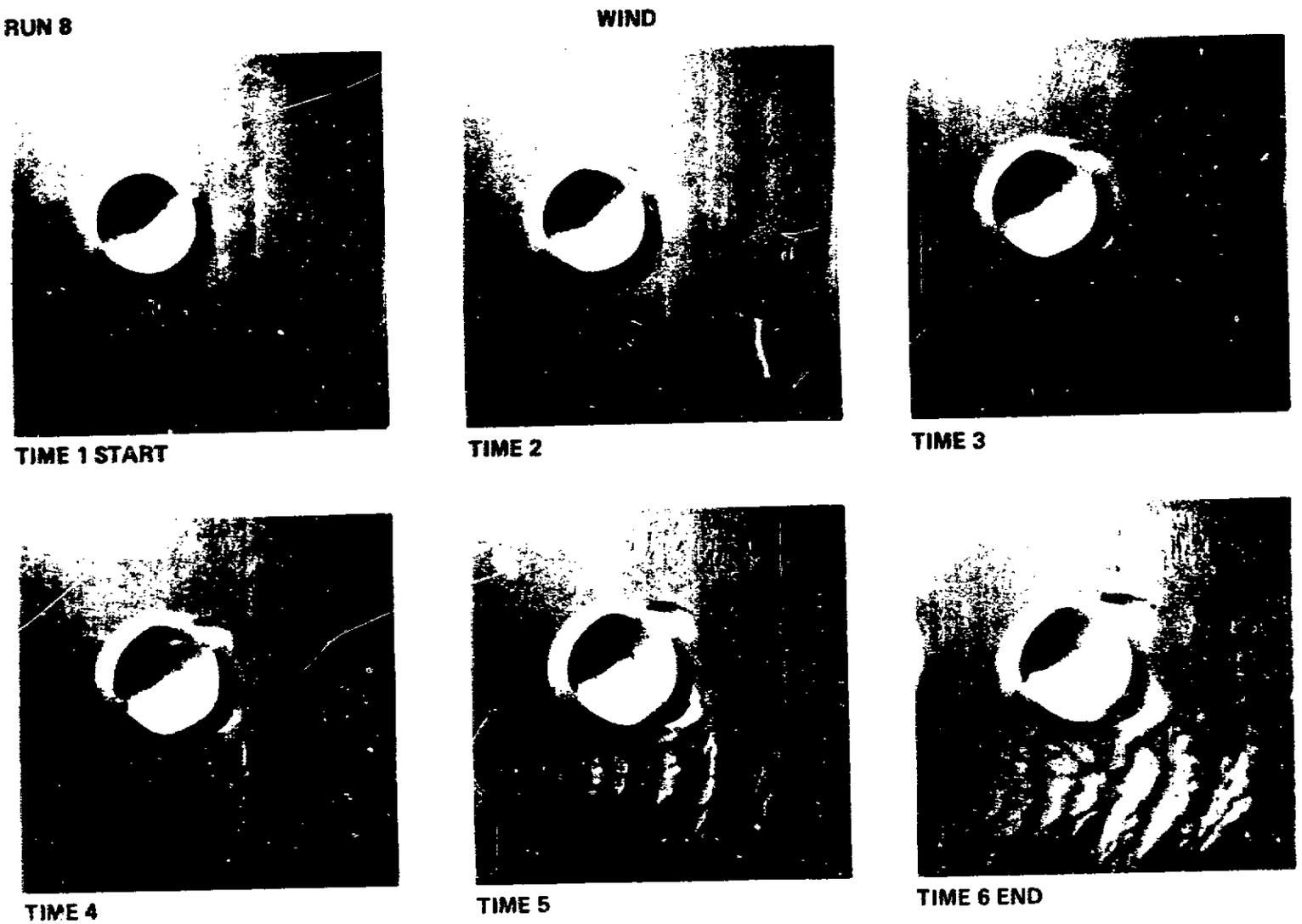

Figure 14. Run 8 wind tunnel simulation of a raised-rim crater molded in loose 120μ sand showing the development of erosional zones on the leeward lateral flanks of the crater.

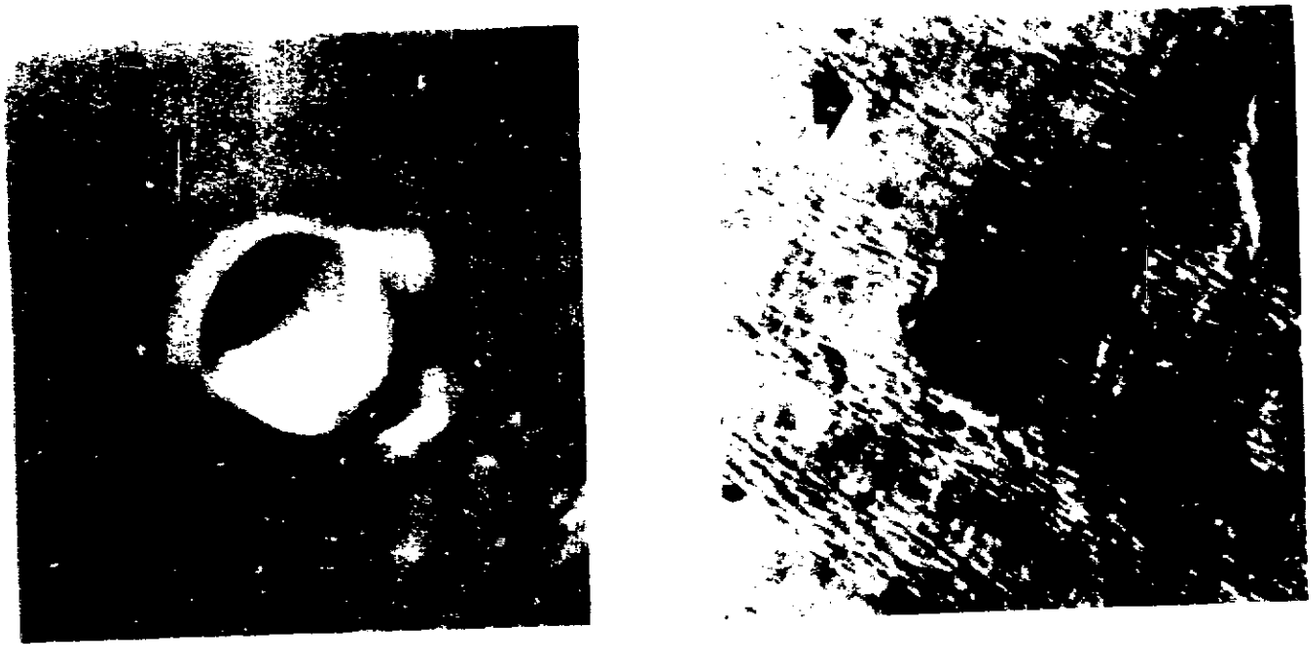

Figure 15. Comparison of Run 8 (figure 14) to a small crater in Mare Tyrrhenum (wind direction arrow determined from other crater streaks in the area). The dark zones on the lateral flanks of the martian crater are in the same position as the erosional zones of Run 8, and its ovoid outline pointing upwind suggests that it similarly has been modified by wind.

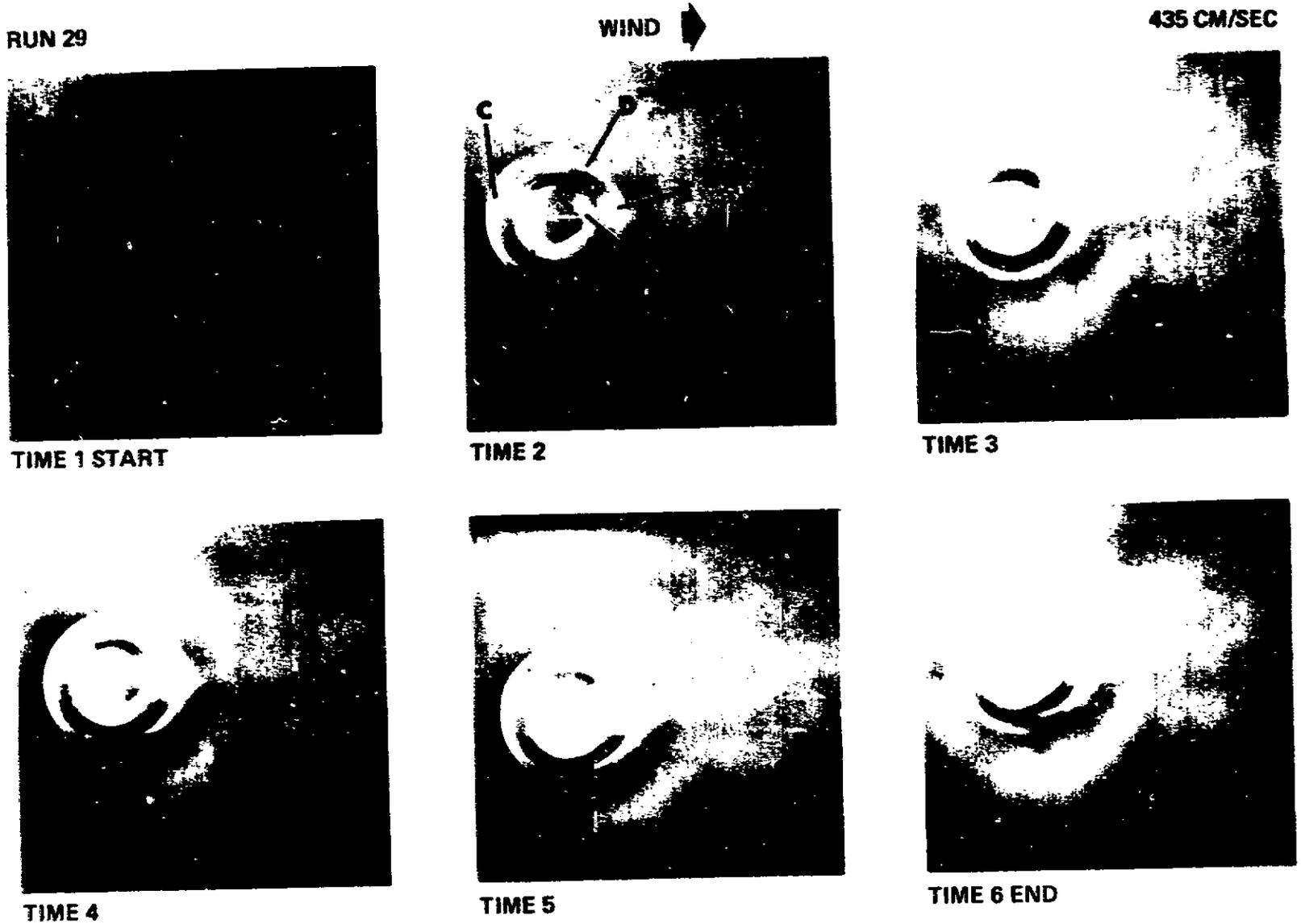

Figure 16. Run 29 for a solid (nonerodible) raised-rim crater model over which loose 120μ sand grains (white material) were blown. Zones of collection are shown at A-E; while arrow indicates reverse flow across crater floor.

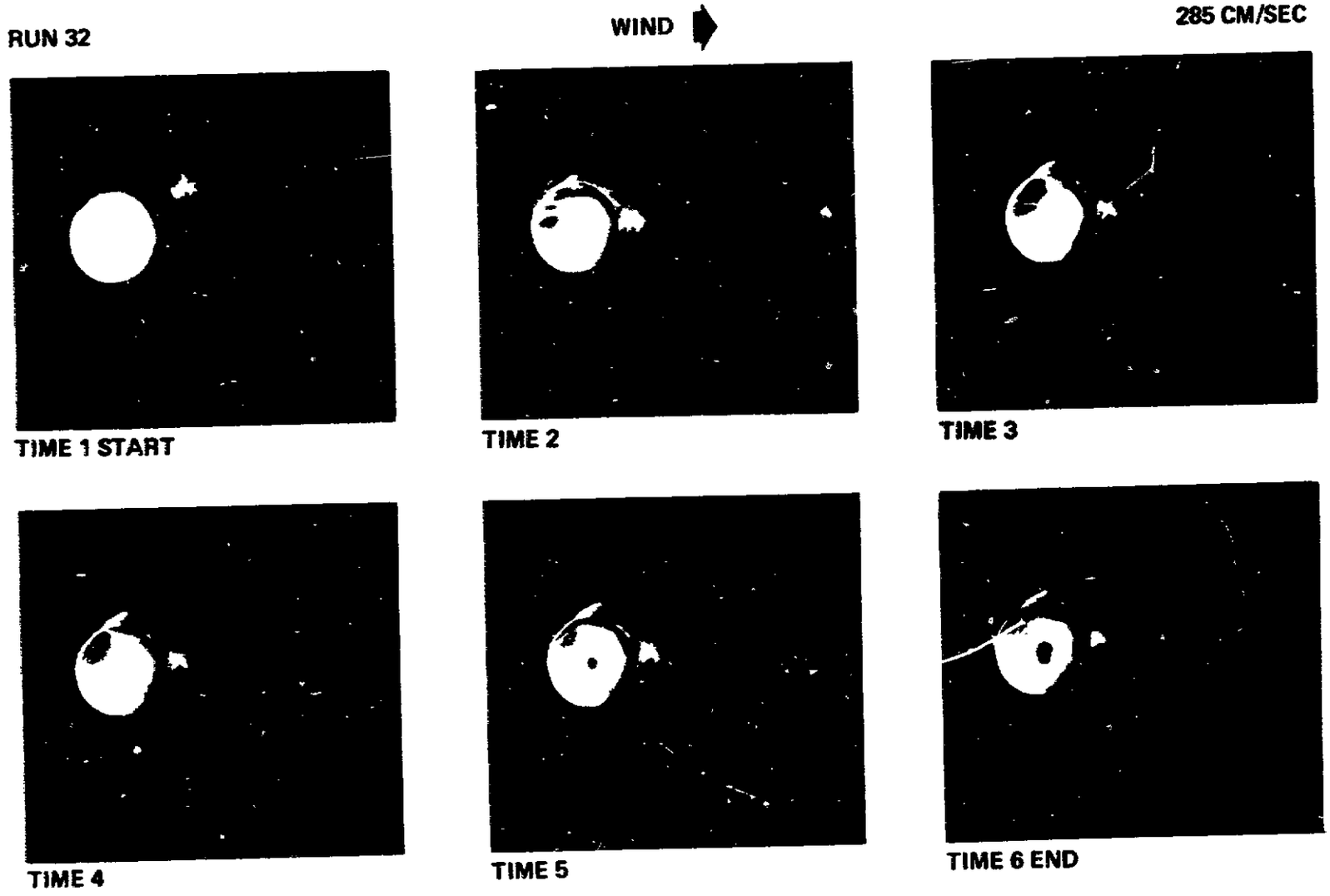

Figure 17. Run 32 for a solid raised-rim crater model in which the crater was filled with loose, 120μ sand to its rims (white material; remainder of model was free of sand) and subjected to wind.

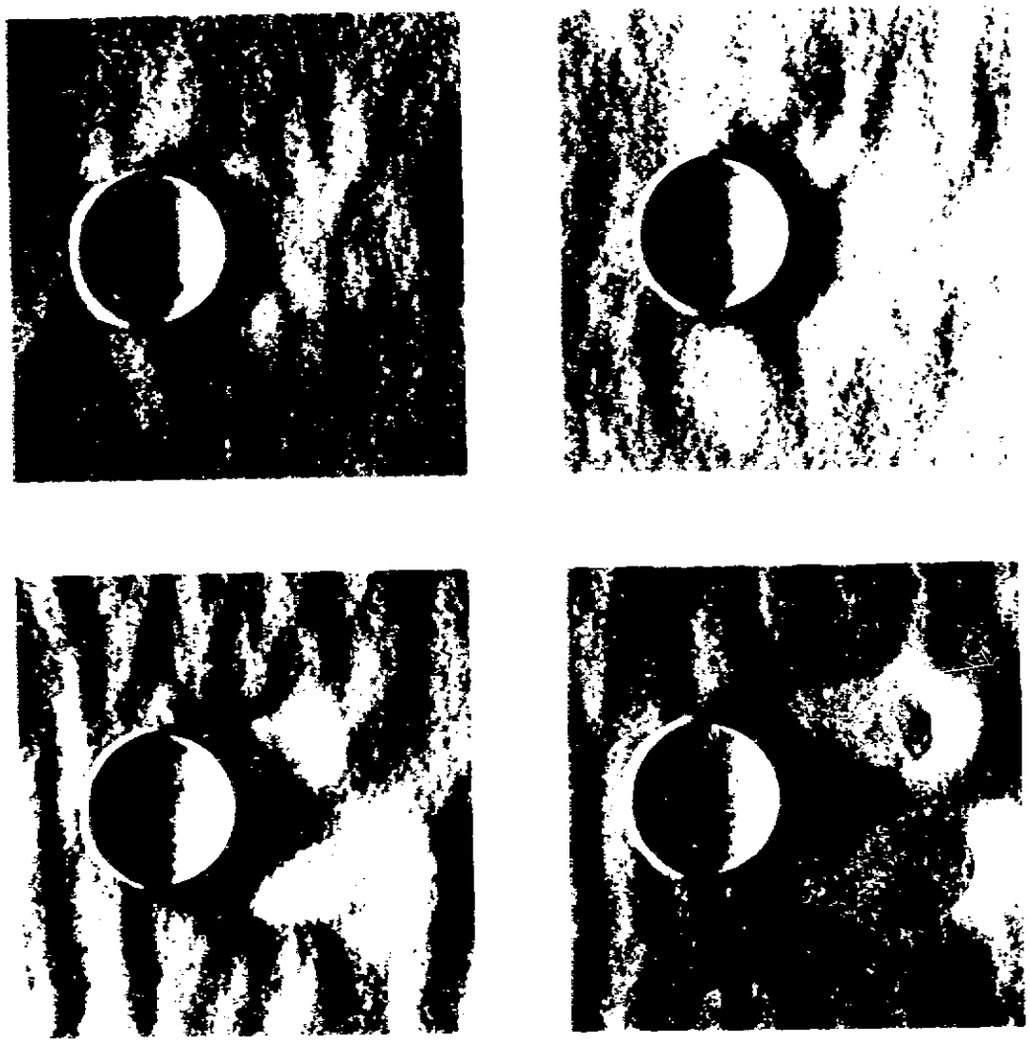

Figure 18. Run I-F-14 for a solid raised-rim crater model in which the surface and part of the crater were covered with a uniform layer of loose 200μ glass particles and subjected to wind.

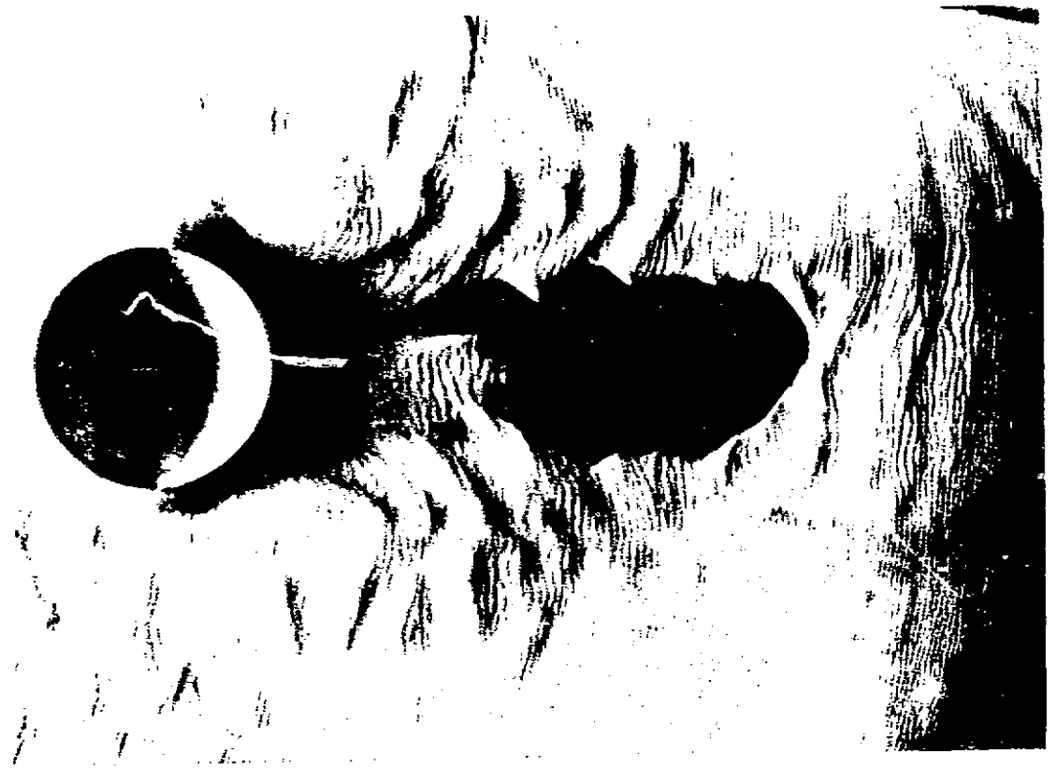

Figure 19. Run I-C16 for a solid raised-rim crater model in which the surface and part of the crater was covered with 91μ glass particles (light material) and subjected to 413 cm/sec wind. Compare to figure 18; at the higher velocity of Run I-C16, the two trailing axial velocity maxima converge and develop a zone of surface stress on the crater wake centerline that is higher than any other place on the flat part of the model, as evidenced by: 1) the cleared area (dark zone) , 2) larger ripples in the particles along the wake centerline than outside the wake, and 3) by direct measurement.

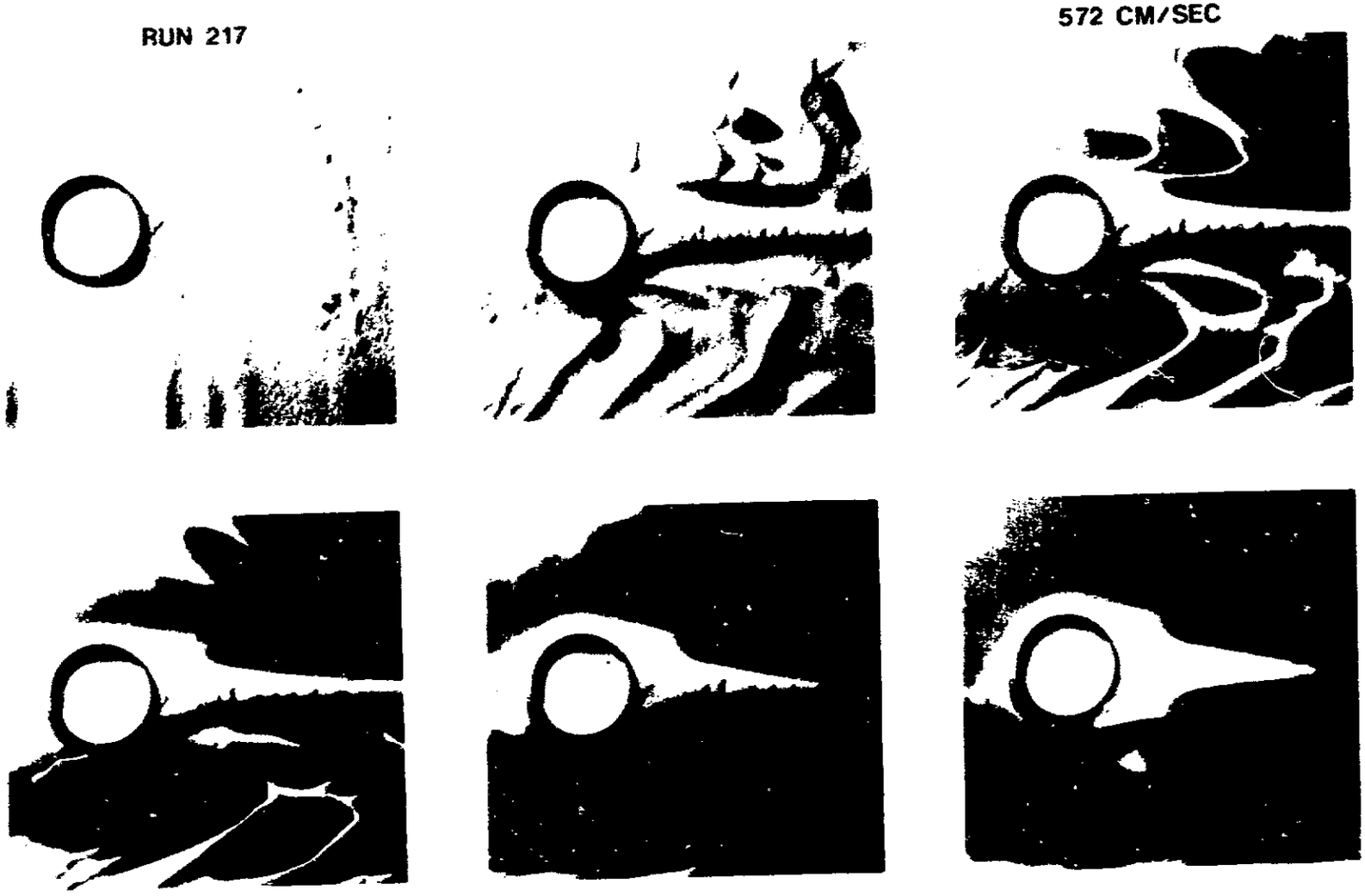

Figure 20. Run 217 for a solid (non-deformable) raised-rim crater model in which the flat surface and all of the crater except the rim were buried with loose 120μ sand.

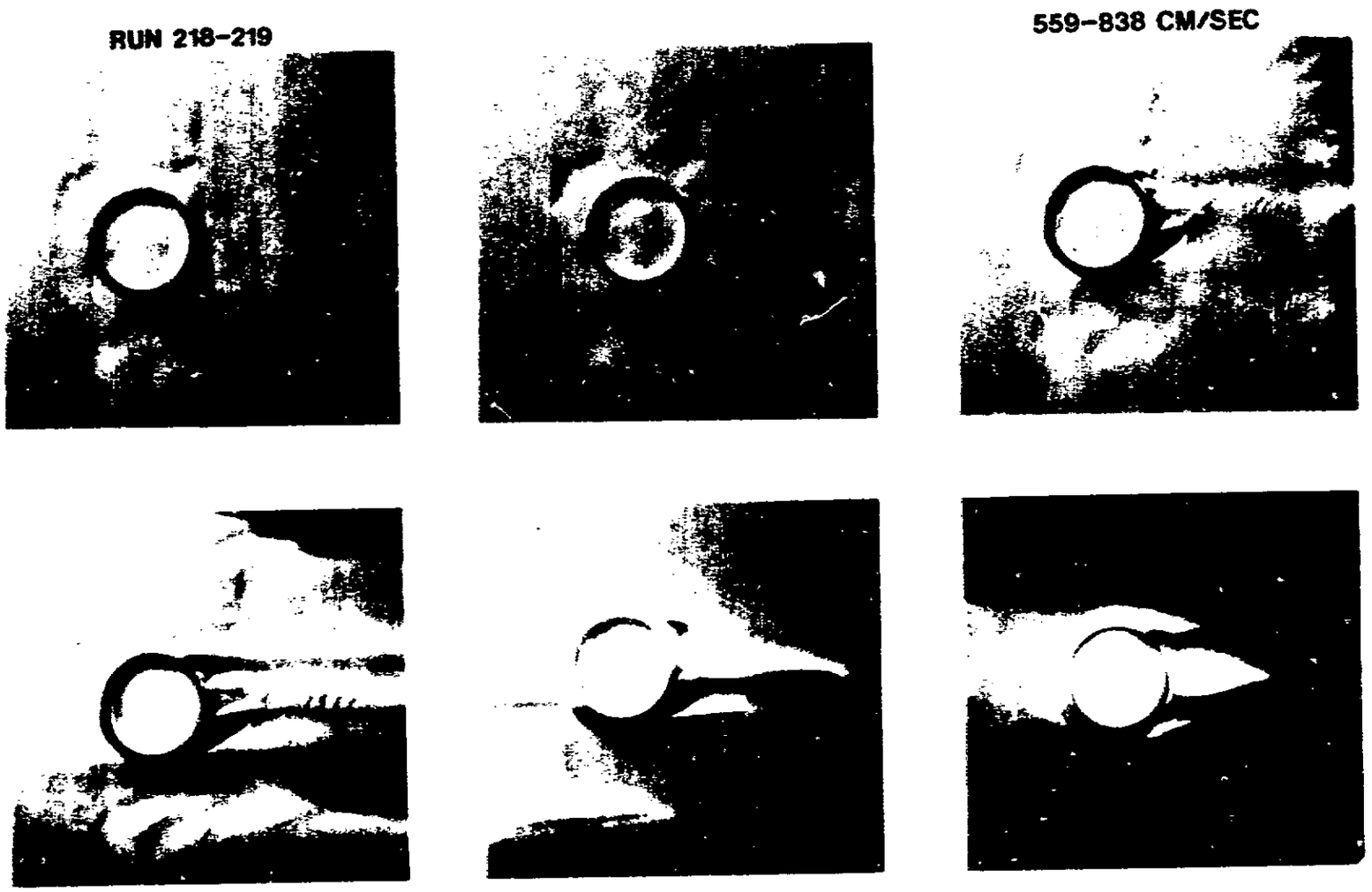

Figure 21 Runs 217-219, with conditions identical to Run 217 (figure 20), except wind velocity which was higher in final frames.

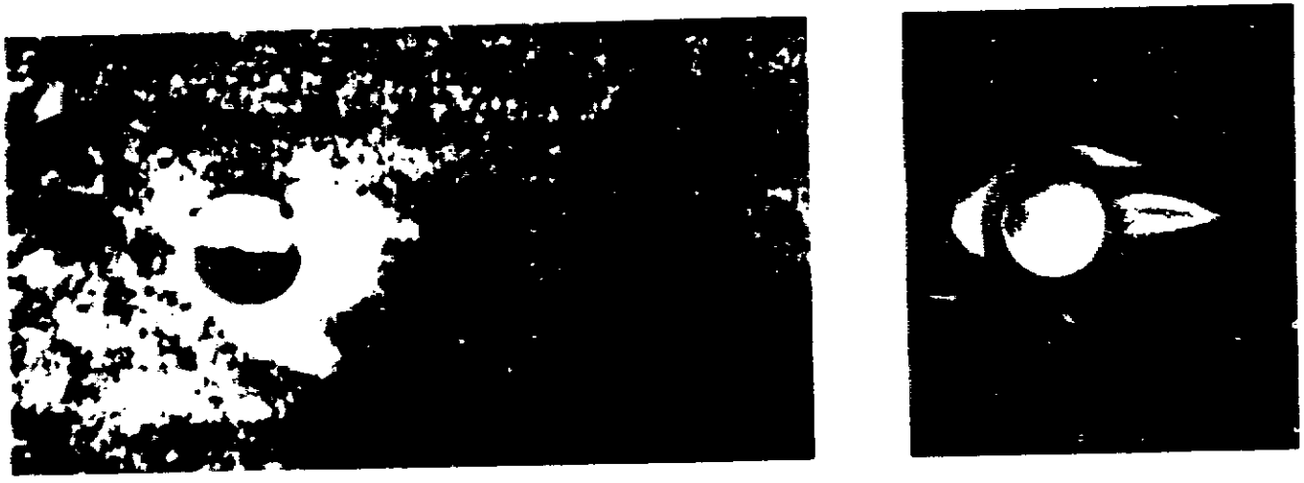

Figure 22. Comparison of Run 219 with a small (2km in diameter) martian crater in the region northwest of Memnonia, showing the similarity of the white streak pattern to the zones of relative deposition of the wind tunnel simulation. Surface wind arrow on the Mariner image was determined from regional streak orientations. Note that the dark zone in the wake of the martian crater (beyond the trilobate white streak) corresponds to the zone of erosion in simulations that result from the confluence of the trailing vortices.

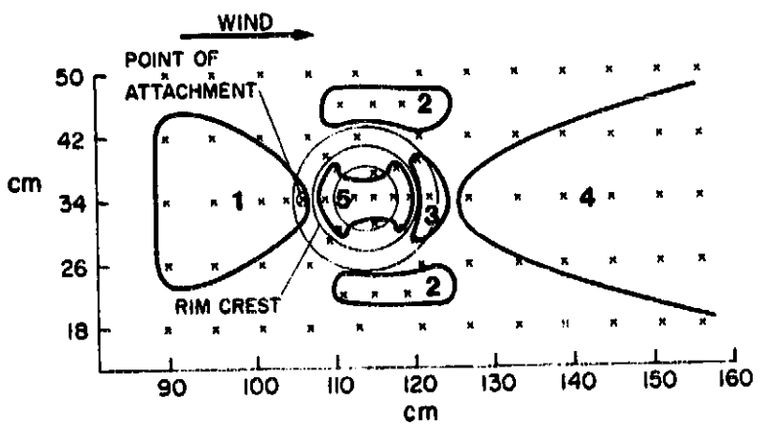

Figure 23. Diagram showing the grid layout for the threshold speed experiments to determine zones of relative erosion and deposition associated with raised-rim craters.

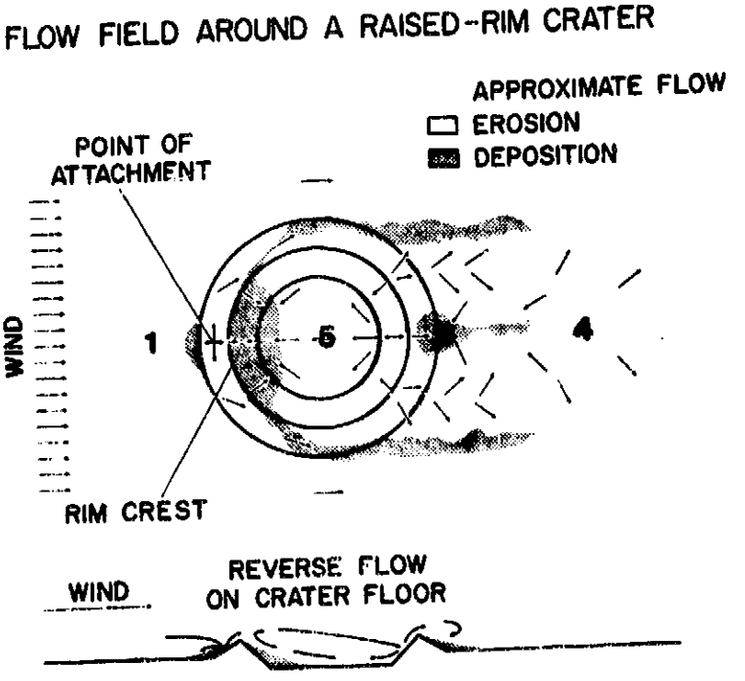

Figure 24. Zones of relative erosion and deposition for a raised-rim crater; arrows represent observed direction of movement of sand.

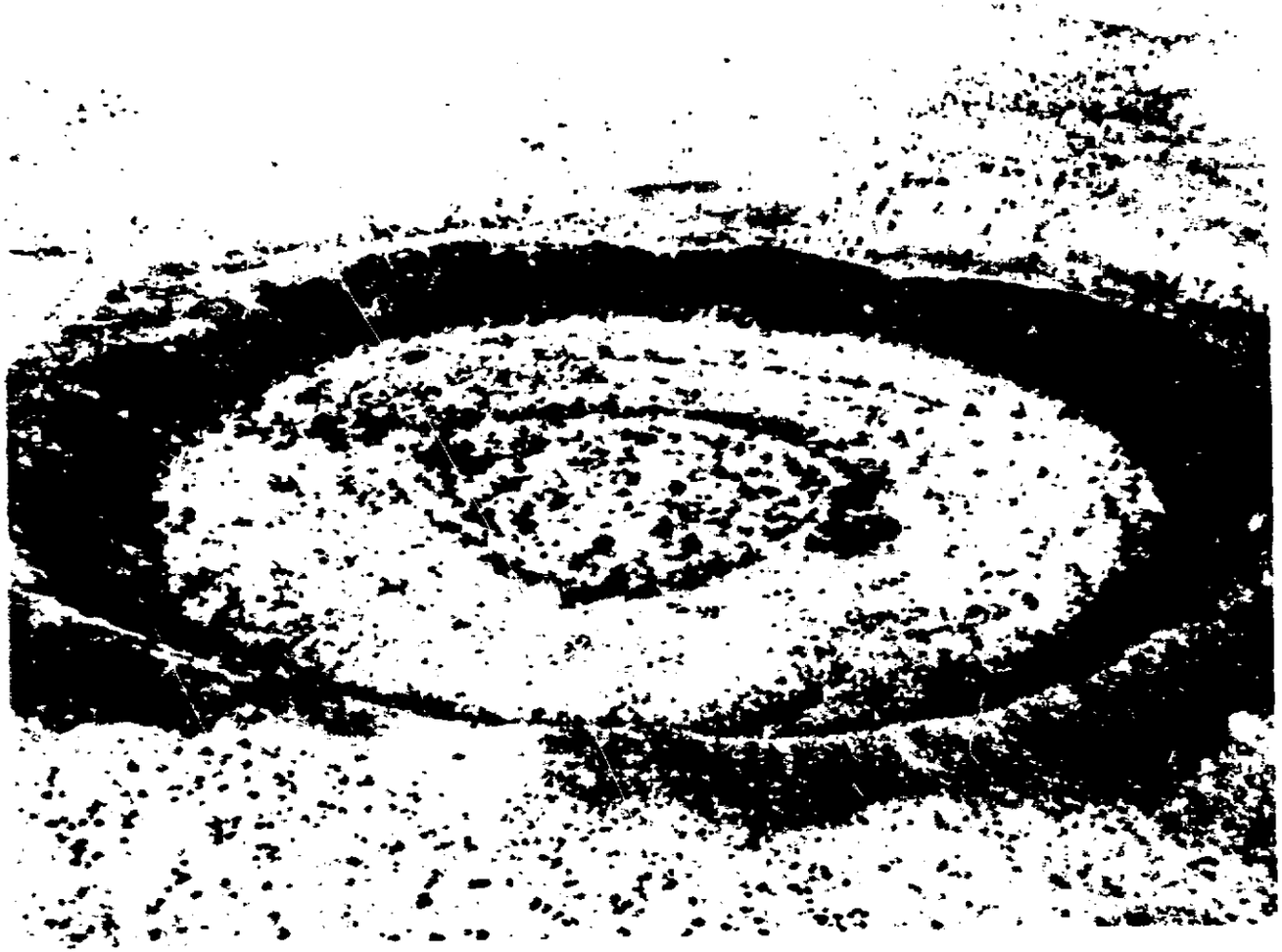

Figure 25. Wolf Creek Crater, Australia, a natural impact crater about 1.2 km in diameter with distinct raised rims. It is situated on flat plains in association with aeolian material and affords the opportunity to observe zones of relative erosion and deposition (form McCall, 1965). View is downwind; rim in foreground shows sand dune over-riding the windward rim.

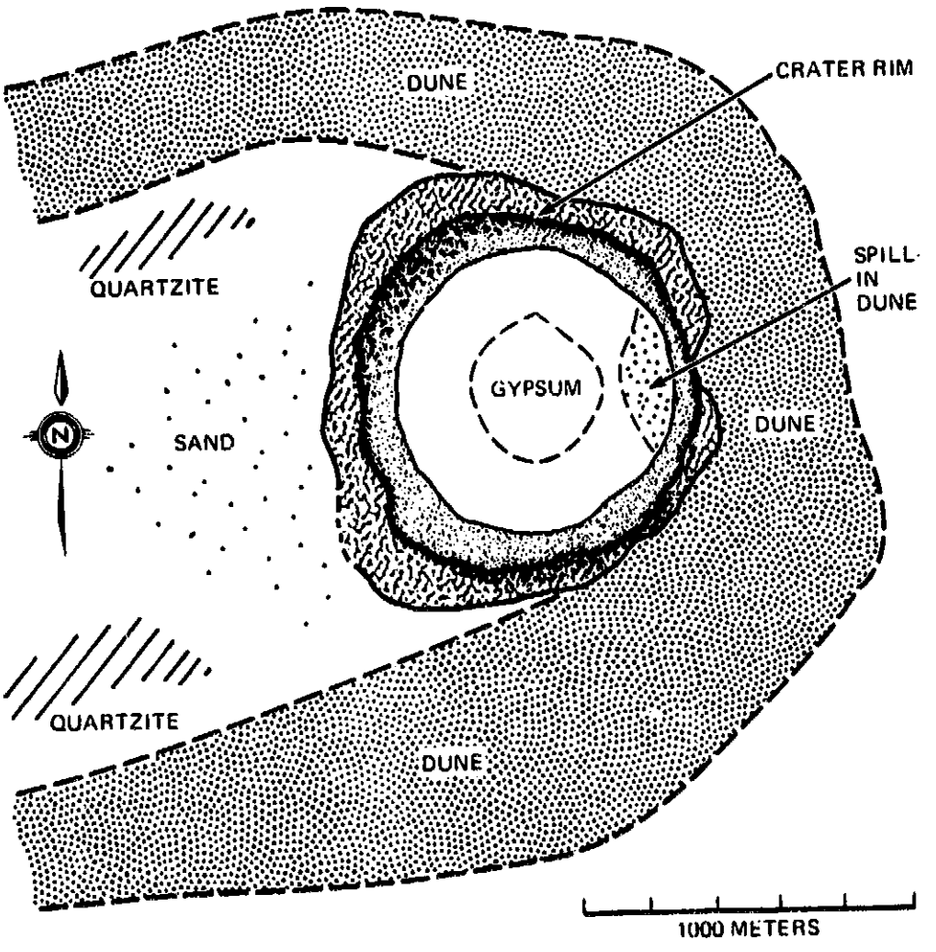

Figure 26. Geological sketch map of Wolf Creek impact crater (from McCall, 1965), showing approximate trilobate pattern of sand deposition around the crater and zones of erosion indicated by bedrock exposures of quartzite. Wind is from right to left (east to west).

Figure 27. Bruneau Sand Dune at Eagle Cove, Idaho. Large dune in center of the 5.6 km basin is about 147 m high and is the result of a bimodal regional wind pattern. Sand is initially deposited in the basin by prevailing northwesterly wind (right side of photograph) and is then maintained in the center of the basin by a secondary southeaserly wind.